The Astrophysical Journal, 572:580–597, 2002 June 10

THE LARGE-SCALE CORONAL FIELD STRUCTURE AND SOURCE REGION FEATURES FOR A HALO CORONAL MASS EJECTION

Tongjiang Wang,[1,2,3] Yihua Yan,[2] Jialong Wang,[2] H. Kurokawa,[3] and K. Shibata[3]

Received 2001 September 14; accepted 2002 February 11

ABSTRACT

On 1998 May 2 a class X1/3B flare occurred at 13:42 UT in NOAA Active Region 8210 near disk center, which was followed by a halo coronal mass ejection (CME) at 15:03 UT observed by *SOHO*/LASCO. Using the boundary element method (BEM) on a global potential model, we reconstruct the large-scale coronal field structure from a composite boundary by *SOHO*/MDI and Kitt Peak magnetograms. The extrapolated large field lines well model a transequatorial interconnecting loop (TIL) seen in the soft X-ray (SXR) between AR 8210 and AR 8214, which disappeared after the CME. The EUV Imaging Telescope (EIT) observed the widely extending dimmings, which noticeably deviate from the SXR TIL in position. We find that the major dimmings are magnetically linked to the flaring active region but some dimmings are not. The spatial relationships of these features suggest that the CME may be led by a global restructuring of multipolar magnetic systems due to flare disturbances. Mass, magnetic energy, and flux of the ejected material estimated from the dimming regions are comparable to the output of large CMEs, derived from the limb events. At the CME source region, Huairou vector magnetograms show that a strong shear was rapidly developed in a newly emerging flux region (EFR) near the main spot before the flare. Magnetic field extrapolations reveal the presence of a " bald patch " (defined as the locations where the magnetic field is tangent to the photosphere) at the edge of the EFR. The preflare features such as EUV loop brightenings and SXR jets appearing at the bald patch suggest a slow reconnection between the TIL field system and a preexisting overlying field above the sheared EFR flux system. High-cadence *Yohkoh*/SXT images reveal a fast expanding motion of loops above a bright core just several minutes before the hard X-ray onset. This may be a precursor for the eruption of the sheared EFR flux to produce the flare. We propose a scenario, similar to the " breakout " model in principle, that can interpret many observed features.

Subject headings: Sun: corona — Sun: flares — Sun: magnetic fields — Sun: particle emission — Sun: UV radiation — Sun: X-rays, gamma rays

On-line material: color figure

1. INTRODUCTION

Coronal mass ejections (CMEs), since first identified with space-borne coronagraphs in the 1970s, have been one of the most extensively studied topics in solar physics because they are a form of largest scale solar activity phenomenon that outputs the material and magnetic flux to interplanetary space, bringing a direct impact on the geomagnetic environment of the Earth. To date a large amount of CMEs in white light have been observed, based on which their properties, such as morphological classification, velocity, mass, kinetic energy, and angular width, are established (e.g., Hundhausen 1997); however, their source region features and associated magnetic structure in the low corona are still lacking comprehensive studies, which are critical for our understanding of the origin of CMEs.

Some recent studies on the joint observations from *SOHO* and *Yohkoh* have begun to reveal these issues. For example, the signatures of CMEs near the solar surface are often associated with filament eruptions (Webb & Hundhausen 1987; Delannée, Delaboudinière, & Lamy 2000; Zhang, Wang, & Nitta 2001), sigmoid-to-arcade events (a preeruption active region structure, initially twisted into an S shape, which evolved into a posteruption cusp-shaped or arcade structure; Hudson et al. 1998; Sterling et al. 2000), and flare-associated ejections of hot plasma with looplike structure around the impulsive phase seen in soft X-ray (SXR; Shibata et al. 1995; Ohyama & Shibata 1998; Nitta & Akiyama 1999). X-ray or EUV dimmings (brightness depletions) are also expected to be the very first signature of CMEs originating in active regions. Double dimming regions are revealed appearing in the concavities of sigmoid-like structures in SXR and EUV at the same time (Sterling & Hudson 1997; Zarro et al. 1999). These observations well support the interpretation that CMEs initiate as eruption of a twisted magnetic rope in the low corona, possibly as the result of a global MHD instability (e.g., Lin & Forbes 2000; Amari et al. 2000).

However, various forms of CME manifestations may not allow one interpretation. For example, multiple CME events can be detected nearly simultaneously at widely separated points (e.g., Lyons & Simnett 1999). Short sequences of major CMEs are related to flares in the same active region without filament eruption associated, and the EUV dimmings appear near the flaring region but also extend to other areas (Delannée et al. 2000; Thompson et al. 2000). Transequatorial loops observed in SXR or EUV that link the principal flaring region and magnetic regions on the opposite side of the equator disappear and become a major compo-

[1] Max-Planck-Institut für Aeronomie, D-37191 Katlenburg-Lindau, Germany; wangtj@linmpi.mpg.de.

[2] National Astronomical Observatories, Chinese Academy of Sciences, 20 Datun Road, Beijing 100012, China.

[3] Kwasan Observatory, Kyoto University, Yamashina-ku, Kyoto 607-8471, Japan.

nent of CMEs (Khan & Hudson 2000; Delannée & Aulanier 1999). During flare CME events, evolution of metric radio emissions reveals that multipolar magnetic systems are connected with the active flare region; the initial instability takes place in a very small volume located at its edge, and then the radio emission sites spread over a large volume in the corona in a timescale of only a few minutes (Pick et al. 1999b; Maia et al. 1999). These observations are difficult to understand by the use of magnetic rope models; instead, they appeared to identify a different type of CMEs that are the results of successive interactions of multipolar magnetic systems leading to a large-scale restructuring (e.g., Pick et al. 1999a). A magnetic breakout model in a quadrupolar topology proposed by Antiochos, Devore, & Klimchuk (1999) has provided such a global destabilization mechanism for multipolar systems involved in both flares and associated CMEs. In addition, based on an observational multipolar structure, Delannée & Aulanier (1999) proposed a scenario showing another possible way to produce flare CMEs by reconnection in magnetic "bald patches" (e.g., Titov & Démoulin 1999).

In this paper, using a field extrapolation method, we reconstruct the large-scale coronal field structure for a halo CME on 1998 May 2, to understand the associated features, such as widely extending EUV Imaging Telescope (EIT) dimmings and SXR transequatorial loop disappearances, from which the possible output of plasma mass and magnetic energy in this CME is derived. Furthermore, we explore the CME origin by analyzing evolutions of the multiwavelength emissions and surface magnetic fields in the source region. In § 2 we describe observations and data reduction. In § 3 we introduce the boundary element method (BEM) for a global potential extrapolation and its application. In § 4 we explore the surface signatures and source region features of the flare CME. We present discussions in § 5 and conclusions in § 6.

2. OBSERVATIONS AND DATA REDUCTIONS

NOAA Active Region 8210 was a remarkable flare-productive region that produced several intense flares and was associated with energetic CMEs during its disk passage at the end of April through the beginning of May in 1998 (Warmuth et al. 2000; Thompson et al. 2000). On 1998 May 2 when the active region was located near the solar disk center (S15°, W15°), the great X1.1/3B flare occurred (Fig. 1*a*). The *GOES* X-ray flux started at 13:31 UT and reached a peak at 13:42 UT. The hard X-ray light curves in three bands (M1: 23–33 keV; M2: 33–53 keV; *H*: 53–93 keV) obtained by the hard X-ray telescope (HXT; Kosugi et al. 1991) aboard *Yohkoh* all showed a very strong impulsive increase at 13:37:20, with its peak count rate in the *H* band above 40 counts s^{-1} per subcollimator. The Hα emissions showed a bright ejection and a Moreton wave (Moreton 1960), generated during the impulsive phase (Warmuth et al. 2000). A sudden decrease of magnetic flux associated with the flare was reported by Kosovichev & Zharkova (1999). The flare was accompanied by a halo CME detected by the Large Angle and Spectrometric Coronagraph Experiment (LASCO; Brueckner et al. 1995) C2 in white light at 15:03 UT (Fig. 1*b*). Manifestations of the radio sources over the solar disk by the Nançay Radioheliograph (NRH) suggested that the CME development may be involved in the large-scale coronal field restructuring (Pick et al. 1999b; Pohjolainen, Khan, & Vilmer 1999; Pohjolainen et al. 2001).

The used data sets include various observations such as magnetograms, Hα images, and EUV and SXR emission images obtained from the photosphere to the corona. The Michelson Doppler Imager (MDI; Scherrer et al. 1995) on board *SOHO* provided full-disk magnetograms taken with a 96 minute cadence and a resolution of 4″. National Solar Observatory (Kitt Peak) (NSO) synoptic maps were produced by magnetograms observed with the spectromagneto-

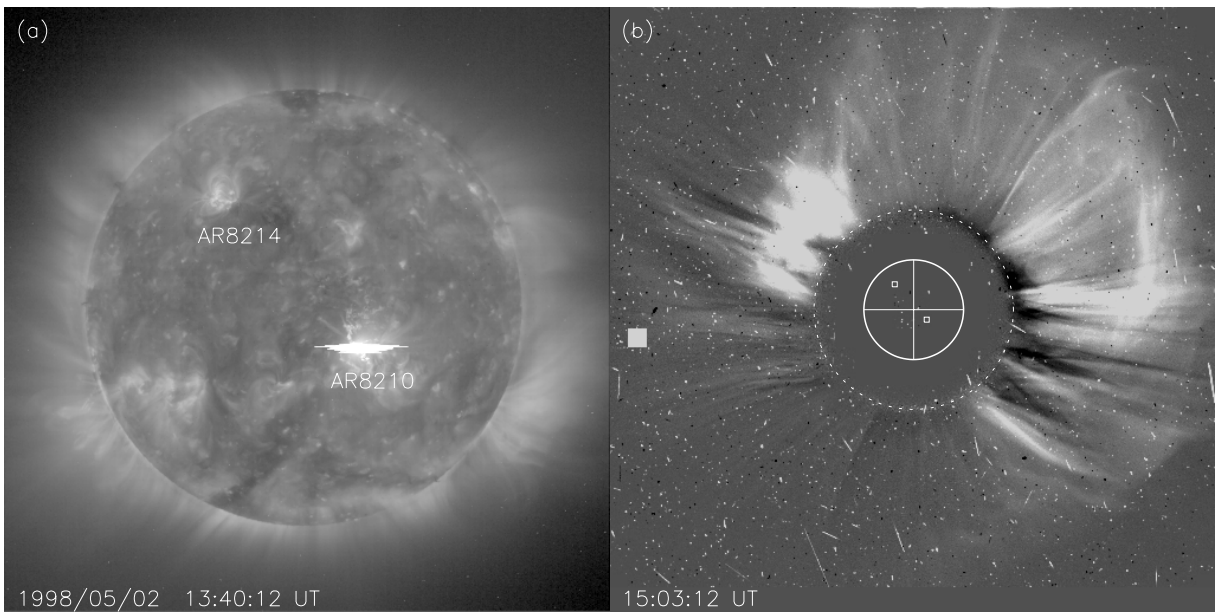

FIG. 1.—(*a*) X1/3B flare observed by *SOHO*/EIT in the 195 Å channel produced by AR 8210 on 1998 May 2 at 13:40 UT. (*b*) Flare-associated halo CME detected by LASCO/C2 at 15:03 UT. A large dashed circle shows the C2 occulting disk with a radius of 2 $R_\odot$, and a small solid circle shows the solar disk where the boxes mark positions of the two major active regions, AR 8210 and AR 8214, shown in (*a*).

graph at the Fe I λ8688 line. The vector magnetograms with a resolution of 2″ were obtained with the Solar Magnetic Field Telescope (SMFT) at the Huairou Solar Observing Station (Ai & Hu 1986; Wang et al. 1996). The line-of-sight and transverse components of the magnetic field are measured at the wing and center of the Fe I λ5324.19 line, respectively. The 180° ambiguity for the transverse field components is resolved with a linear force-free field method to best fit the azimuth (Wang & Abramenko 2000). The Huairou vector magnetograms are favorable to analyses of the magnetic nonpotential feature and topological connectivity of active regions (Wang, Xu, & Zhang 1994; Wang, Wang, & Qiu 1999). The Hα observations of an X1.1/3B flare were made at the Kanzelhöhe Solar Observatory (Warmuth et al. 2000). The EUV images were obtained by EIT (Delaboudinière et al. 1995) on board *SOHO* in the 195 Å channel centered on Fe XII emission lines, best exhibiting the development of the CMEs by following the dimmings in the low ($<1.2\ R_\odot$) corona (e.g., Dere et al. 1997). The soft X-ray telescope (SXT; Tsuneta et al. 1991) on *Yohkoh* recorded the SXR emissions of hot plasmas in the low corona.

For co-alignments with the MDI image, an SXT partial-frame image is first co-aligned to the full-frame image obtained closest in time to determine its position on the solar disk, then derotated to the time of a full-disk magnetogram used in this study. Finally, a patch of the MDI image of the same size is cut out at the position of the co-aligned SXT image. The co-alignments of Hα images with SXR and MDI images are made in the same way. The above co-alignments have an accuracy of about 5″. In light of the correspondence between a bright point (BP) and a bipole of magnetic elements, co-alignments of the data sets of SXT, EIT, and MDI are improved up to 3″ at AR 8210. The exact disk positions (errors of less than 2″) for the Huairou vector field data are obtained from a comparison with MDI magnetograms by applying the cross-correlation, allowing coordinated analyses between Huairou data and the others. In addition, the Huairou data are divided by a factor of 3, to correct system difference in calibrations from MDI data. This factor is obtained by measuring a ratio of the total fluxes for identical magnetic structures observed by the two systems.

3. CALCULATIONS OF THE LARGE-SCALE CORONAL MAGNETIC FIELD

When the magnetic field in an area larger than an active region is studied, the curvature of the solar surface should be taken into account. The problem of calculating the solar global magnetic field on the assumption of the potential field above the photosphere can be treated in the spherical harmonic expansion method (Newkirk, Altschuler, & Harvey 1968; Altschuler & Newkirk 1969) or the Green's function method (GFM; Schatten, Wilcox, & Ness 1969; Sakurai 1982) by solving Laplace's equation, which satisfies the boundary condition specified by the observation (e.g., measurements of the line-of-sight component of the photospheric magnetic field collected over a solar rotation). In order to simulate the effect of the solar wind on the coronal field, a zero-potential surface at about 2.5 $R_\odot$ (the so-called source surface) is assumed in common (e.g., Altschuler & Newkirk 1969). In this section we introduce a different method, which can also deal with the above problem provided that the radial component of the field over the solar surface is supplied (e.g., by assuming the radial field approximation in Newkirk et al. 1968 and Schatten et al. 1969). We further show an application of this method to our studied case.

3.1. *Boundary Integral Method*

Under the current-free condition ($\nabla \times \boldsymbol{B} = 0$), the coronal magnetic field can be represented by a scalar potential Ψ as follows:

$$\boldsymbol{B} = -\nabla\Psi\ , \tag{1}$$

$$\nabla^2\Psi = 0\ . \tag{2}$$

Let Ω be the open space above the Sun and $\Gamma_\odot$ the photospheric surface, and assume that the Neumann boundary condition is posed on $\Gamma_\odot$, i.e.,

$$-\frac{\partial\Psi}{\partial n} = B_n \quad \text{on } \Gamma_\odot\ , \tag{3}$$

where B_n is the field component inward normal to the solar surface (i.e., $B_n = -B_R$, where B_R is the radial field component).

The condition at infinity is

$$\Psi(R) = O\left(\frac{1}{R}\right), \quad \text{when } R \to \infty\ , \tag{4}$$

where R is the radial distance from the Sun. Equations (2), (3), and (4) constitute an exterior boundary value problem. In the case that the effect of solar wind is considered, a condition of the source surface Γ_s is imposed at $R \approx 2.5\ R_\odot$ by

$$\Psi = 0 \quad \text{on } \Gamma_s\ , \tag{5}$$

as a result of which the field lines become purely radial on this surface as described by Altschuler & Newkirk (1969). Equations (2), (3), and (5) make up a similar exterior boundary problem to that of equations (2), (3), and (4). For both cases, the solution of Laplace's equation can be written as a boundary integral equation representation by applying Green's second identity (Courant & Hilbert 1962; Arfken 1966), when a reference function is considered as

$$F = \frac{1}{4\pi r}\ , \tag{6}$$

where r is the distance between a variable point and a fixed point i, both in Ω. A similar treatment has been applied for resolving steady state and linear electromagnetic field problems (Yan, Yu, & Shi 1993) and also the force-free field problems (Yan, Yu, & Kang 1991; Yan & Sakurai 2000). We find that the potential at any point i in the infinite boundary case is

$$c_i\Psi_i = \oint_{\Gamma_\odot}\left(-FB_n - \Psi\frac{\partial F}{\partial n}\right)dS\ , \tag{7}$$

while in the source surface case

$$c_i\Psi_i = \oint_{\Gamma_\odot}\left(-FB_n - \Psi\frac{\partial F}{\partial n}\right)dS + \oint_{\Gamma_s}\left(F\frac{\partial\Psi}{\partial n}\right)dS\ , \tag{8}$$

where c_i is a constant depending upon the location of the point i; $c_i = 1$ if point i is in volume Ω, and $c_i = \frac{1}{2}$ if point i is on smooth surface $\Gamma_\odot$ (or Γ_s). The normal derivative is

defined as

$$\frac{\partial}{\partial n} dS \equiv \frac{\partial}{\partial r}\frac{\partial r}{\partial n} dS = \frac{\partial}{\partial r}\left(\frac{\boldsymbol{r}}{r} \cdot \boldsymbol{n}\, dS\right), \quad (9)$$

where $\boldsymbol{r}/r$ is the unit vector from a variable point to a fixed point i and $\boldsymbol{n}$ is the normal direction of dS.

To determine the potential in Ω requires first of all knowledge of the values of Ψ over $\Gamma_\odot$ in equation (7) and secondly knowledge of both Ψ over $\Gamma_\odot$ and $\partial\Psi/\partial n$ over Γ_s in equation (8). If we consider the integral equation (7) or equation (8) in the case of the point i on the boundary, these required quantities can be numerically solved with the help of the BEM (Brebbia, Telles, & Wrobel 1984; Yan et al. 1993; Yan & Sakurai 2000) as long as B_n are offered in the observation. Thus, the field $\boldsymbol{B}$ at any point in Ω can be specified by using equation (1) with equation (7) or equation (8) as follows:

$$\boldsymbol{B} = \oint_{\Gamma_\odot} \left[B_n \frac{\partial F}{\partial \boldsymbol{r}} + \Psi \frac{\partial}{\partial \boldsymbol{r}} \left(\frac{\partial F}{\partial n}\right)\right] dS \quad (10)$$

in the infinite boundary case and

$$\boldsymbol{B} = \oint_{\Gamma_\odot} \left[B_n \frac{\partial F}{\partial \boldsymbol{r}} + \Psi \frac{\partial}{\partial \boldsymbol{r}} \left(\frac{\partial F}{\partial n}\right)\right] dS - \oint_{\Gamma_s} \left(\frac{\partial \Psi}{\partial n}\frac{\partial F}{\partial \boldsymbol{r}}\right) dS \quad (11)$$

in the source surface case, where Cartesian coordinate system (x, y, z) is taken with the origin at the center of the Sun, $\partial/\partial \boldsymbol{r} \equiv (\partial/\partial x, \partial/\partial y, \partial/\partial z)$, and $\boldsymbol{B} = (B_x, B_y, B_z)$.

3.2. *Reconstructions of the Magnetic Structure of 1998 May 2*

The global field extrapolation based on synoptic maps of the photospheric magnetic field has been widely used to study the long-lived coronal phenomena such as the solar wind (e.g., Hakamada & Kojima 1999). However, when the transient magnetic activity such as flares or CMEs is concerned, because they are often associated with shorter timescale magnetic features such as small-scale flux emergence and cancellation that change magnetic fields in active regions considerably in a few days or even hours, a single magnetogram-based extrapolation is much recommended, even for the large scale when some special treatments to the boundary are made. For example, Poletto & Kopp (1988) periodically extended the data within a longitude span of 60° to the whole solar surface. Sakurai (1982) assumed the magnetic field distribution on the invisible solar hemisphere to be the mirror reflection of that of the visible hemisphere. Zhao, Hoeksema, & Scherrer (1997) inserted the daily magnetogram of interest into the synoptic map.

Here we take the last method to construct a special synoptic map with its central Carrington longitude corresponding to the central meridian of the single magnetogram (see Fig. 2*a*). In order to accommodate a higher spatial resolution in the computation, our numerical boundary is taken only within an equatorial zone of 60°, with the grid resolutions of 1° × 1° in the inserted part and about 1.°2 × 1.°2 in the other part. We neglect the polar regions because the magnetic field is weaker, giving only a small contribution to the boundary integral in equations (10) and (11). Since the MDI provided full-disk magnetograms with a plate scale of 2″ pixel^{-1}, while the grid scale 1° corresponds to 7″–16″ in the inserted region, we first make a 5 × 5 pixel smooth on the MDI data and then interpolate nodal values. Figures 2*b* and 2*c* demonstrate that the projected spherical mesh points can cover main magnetic structures in active regions AR 8210 and AR 8214, and the total magnetic flux for these two regions is well maintained after the smoothing and discretizing processes (see Table 1). By the BEM described in the last section, both the geometry and functions (the field and the potential) on each element are approximated by nine-point biquadratic-shape functions, which effectively reduce the effect of numerical discretization on the BEM calculations (Yan et al. 1993). Furthermore, we make some assumptions in order to apply the BEM. First, we give up considering the source surface as a result of the computer's capacity; this assumption is reasonable for the calculation of the low coronal field. Second, we simply regard the line-of-sight component of the observed fields as the radial component instead of deriving it by assuming the radial field approximation (Newkirk et al. 1968), which is invalid in active regions.

In the practical calculation, we find that the calculated field near the boundary surface (at heights of a scale less than the nodal interval of ~0.017 $R_\odot$) tends to be bumpy, as a result of the singular integrals. This problem can be solved generally by employing a Gaussian integration scheme over subdivided elements (Yan et al. 1993). Considering the accuracy and computing time, we calculate the field lines starting from the height of 0.02 $R_\odot$ and ending at 0.015 $R_\odot$. For a comparison, field extrapolations are performed for two boundary cases, one based on a single magnetogram and the other on a composite synoptic map (see Fig. 3). The calculated field line patterns show the following features. (1) Near the limb most of the open field lines (defined as those with height $H \geq 1.5\ R_\odot$) in the former case become closed in the latter one, e.g., at the disk northeast, northwest, and south. (2) In the two cases the closed field lines with the height within 0.5 $R_\odot$ have similar connectivity, especially at the disk center. The coefficients of the Spearman rank correlation (Press et al. 1994) are calculated for the height (H), the separation (D), and the length (L) of these closed field lines, listed in Table 2. The results show that the correlation is well above 0.9 for the low coronal field lines ($H \leq 0.2$ or 0.5 $R_\odot$) while about 0.7 for those low and large-scale ones ($D \geq 0.2\ R_\odot$). Thus, when the studied objects are located close to the disk center and limited in the low corona, the single-magnetogram choice may be good enough for field calculations, which can save much computing time.

In addition, Figure 3 shows intriguing connectivities for the northeast loops of AR 8210. They look as if the positive polarities at the north of the main magnetic structure of AR 8210 (see Fig. 2*b*) were negative. This is due not to the mesh precision but to the choice of the field line footpoints at 0.02 $R_\odot$, where the positive flux has decayed to a very small value. For this region, we measure the total flux of 1.83×10^{21} Mx from the MDI magnetogram and 1.86×10^{21} Mx from the mesh nodes; the total fluxes of the calculated field are 1.87×10^{20}, 1.65×10^{19}, and 0 Mx at heights of 0.01, 0.02, and 0.03 $R_\odot$, respectively.

4. ANALYSES OF SURFACE FEATURES OF THE FLARE CME

4.1. *On the Large Scale*

4.1.1. *EIT Dimmings*

The *SOHO*/EIT in the 195 Å channel observed an X1/3B flare in AR 8210 at 13:40 UT (see Fig. 1) and detected dimming features first at 14:10 UT, while LASCO C2

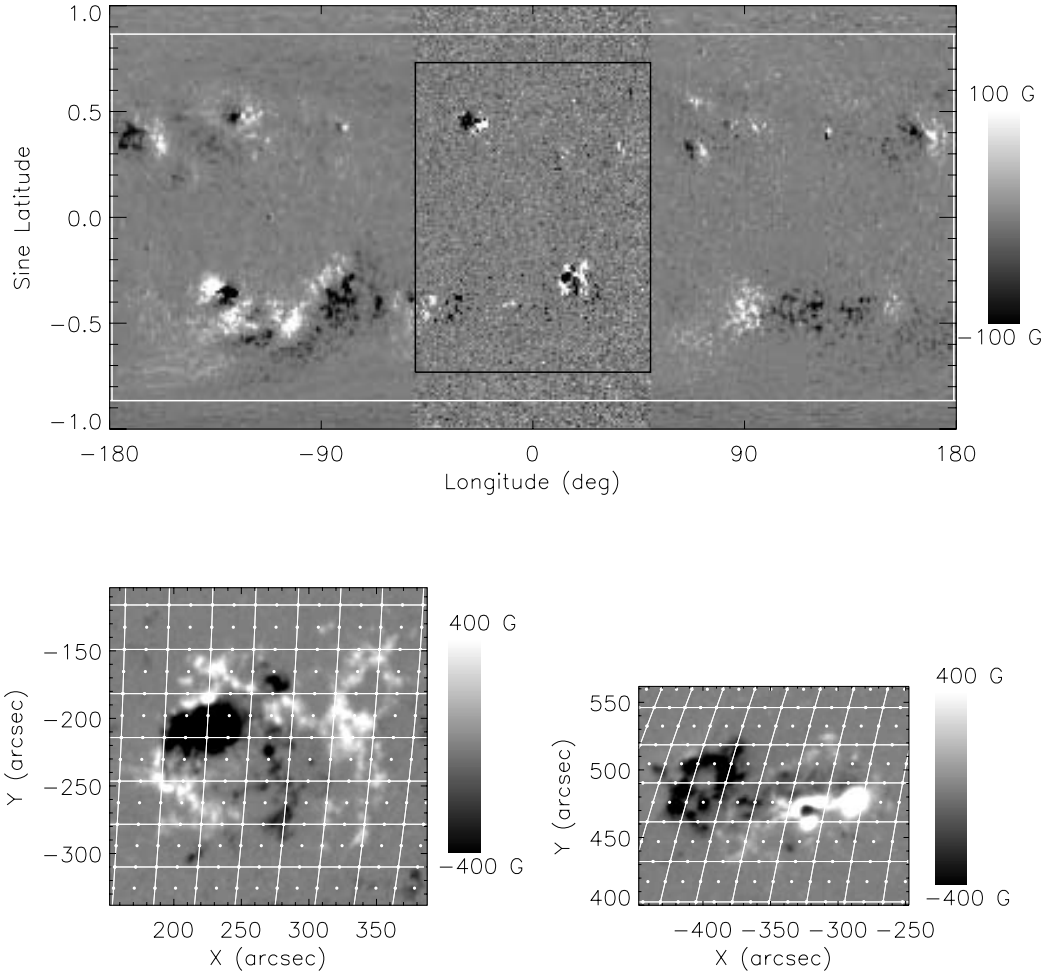

FIG. 2.—*Top:* Composite synoptic magnetic map in rotation 1935/6 using Kitt Peak data and full-disk MDI data at 12:48 UT on 1998 May 2. The black box shows the inserted region of interest covering 50° of the central meridian passage and 47° of the equator, where numerical calculations use the higher grid accuracy (1° × 1°) than in the other region (about 1.°2 × 1.°2) within an equatorial zone of 60° shown in the white box. *Bottom:* MDI magnetograms for AR 8210 and AR 8214 taken at 12:48 UT, overlaid with the projected spherical 1° × 1° mesh, which demonstrate 3 × 3 point biquadratic elements used in BEM calculations. Cartesian coordinates in the bottom panels have the origin at the solar center.

detected the appearance of a CME in white light at 14:06 UT (Thompson et al. 2000). The difference images, produced by referring to a preflare image at 13:20 UT, show that the dimmings spanned a very large scale from the flaring region extending to the nearby region of AR 8214 over about 60° in latitude and 45° in longitude (see Figs. 4*c* and 4*d*). The main dimmings, R1 and R2, decayed a little over about 2 hr, indicating that these places might undergo a substantial density depletion during the flare. It is also found that some dimmings, for example, Ra and Rb, were still developing after the flare (see Fig. 4*d*).

TABLE 1

TOTAL MAGNETIC FLUX OF AR 8210 AND AR 8214 MEASURED FROM THE ORIGINAL MDI DATA AND DISCRETIZED MESH DATA SHOWN IN FIGURES 2*b* AND 2*c*

	AR 8210		AR 8214	
DATA	Φ^+ ($\times 10^{21}$ Mx)	Φ^- ($\times 10^{21}$ Mx)	Φ^+ ($\times 10^{21}$ Mx)	Φ^- ($\times 10^{21}$ Mx)
MDI	9.62	12.0	6.17	7.10
MESH	9.98	11.5	6.25	7.76

NOTE.—The calculations of the total flux for both MDI and mesh data are based on the spherical geometry and taking a cutoff as 20 G.

The potential extrapolation shows that the large-scale field lines with one end anchoring at the flaring region, AR 8210, connect to widespread regions, such as AR 8214, the quiet region (QR), the magnetic pore (MP), and the western limb (see Fig. 4*a*). It also shows some open field lines anchoring at AR 8210 and its eastern region. Measurements of the total flux for AR 8210 (see Table 1) reveal that this active region shows the distinct flux imbalance; its total net flux is about -2.4×10^{21} Mx. This strong flux imbalance is highly favorable for the interconnecting fields forming between the super AR 8210 and the other magnetic regions, but it should point out that a strong flux imbalance is generally not sufficient for such connections between two active regions as a result of the potential effects of close active regions in the same hemisphere and of the polar fields. Figure 4*c* shows that the dimmings well coincide with the footpoint regions of computed field lines, for example, R1, R2,. . ., R6. The major dimmings are directly related to the flaring region by the field line connections, for example, R1, R2, and R4. The part of dimming R2 is also linked with AR 8214. The other dimmings, for example, R3, R5, and R6,

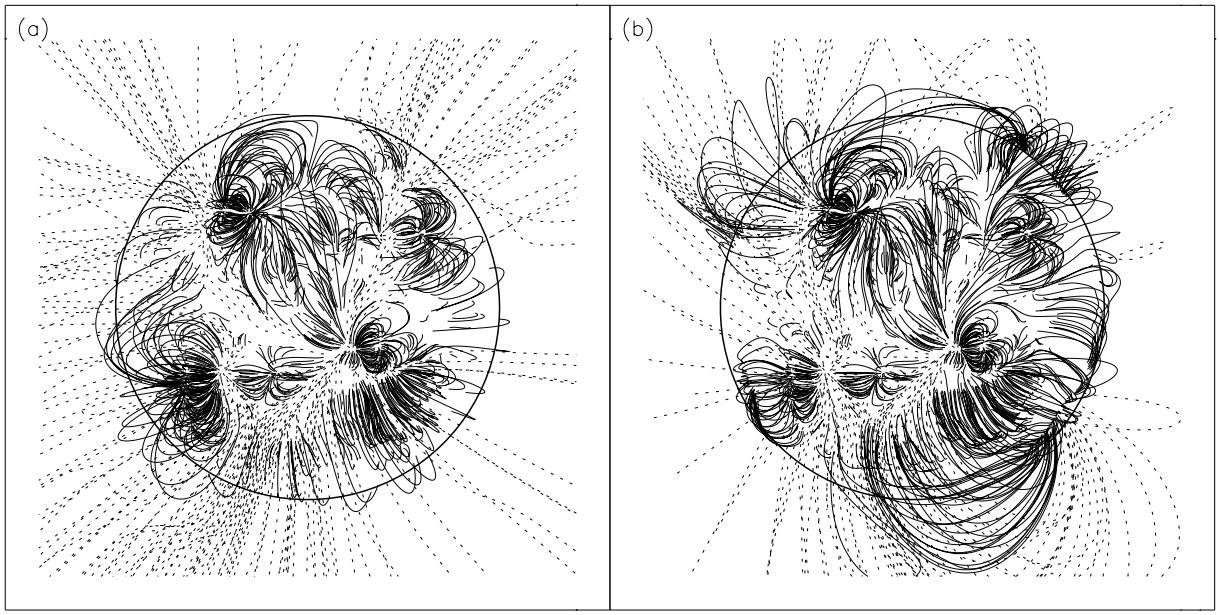

FIG. 3.—Potential field line maps calculated by using the BEM for two kinds of the boundary cases: (*a*) the large-scale central patch of a single full-disk magnetogram, framed by a black box in Fig. 2*a*, and (*b*) the equatorial zone of a composite synoptic map, framed by a white box in Fig. 2*a*. The field lines start from the height level of 0.02 $R_\odot$ above the photospheric surface; the solid lines represent the closed field lines with height less than 0.5 $R_\odot$, and the dashed lines represent the other closed or open field lines.

correspond to the negative flux regions with the same polarity as the net flux of AR 8210, so they are not directly linked to the flaring region, but we notice that they are linked with those immediately flare-related dimmings, for example, R3 → R2 or R5 → R4. Dimming R6 is very peculiar, which is linked with the open field lines and appeared early in the impulsive phase shown in Figure 4*b*.

In order to make quantitative analyses, we demarcate the dimming regions by taking those pixels of the intensity decrease above $N_d\sigma$, where N_d is a factor and σ is the noise level in the difference image. For convenience, we call N_d the "dimming depth." Figure 5 shows variations of the area of the dimmings and the contained total flux of certain polarity with respect to the dimming depths. We find that most of the dimmings are dominated by certain magnetic polarity, and this tendency increases with the dimming depth. The dimmings closer to the flaring region appear "deeper" than those farther away, for example, R1 is deeper than R2. The unipolar feature of dimmings is consistent with their spatial relationship with footpoints of the field lines.

If the dimmings are considered to result from the coronal plasma evacuation at their footpoints as magnetic loop systems rapidly open or expand, a substantial fraction of the CME mass could come from the low corona in the dimming regions (Hudson, Acton, & Freeland 1996; Sterling & Hudson 1997). We estimate the preflare mass and "frozen-in" magnetic energy in the dimming regions, by taking the volume with a height range from 0.01 to 0.2 $R_\odot$ and assuming a hydrogen plasma with equal proton and electron number densities, and the potential field distribution. In a region of interest, we define the substantial dimming regions with intensity decrease above 3 σ (see Fig. 4*c*) and measure their total area in a spherical geometry. We obtain the total area of the dimmings, $A \sim (1.2 \pm 0.8) \times 10^{11}$ km^2, where the error $\Delta A = A_{2\sigma} - A_{3\sigma}$. We divide the dimming volume into 20 layers, apply the data of electron density for the equatorial region of maximum cycle corona in the models of Zheleznyakov (1970) and Arthur (2000), and then obtain a total mass of (6–11) $\times 10^{15}$ g for the dimming regions (see the second column of Table 4). They are consistent with estimates of typical CME masses from coronagraph observations ranging from 10^{15} to 10^{16} g (e.g., Kahler 1992). For the same dimming volume and using the same layer divisions for a height scale of 0.01–0.2 $R_\odot$, we calculate the total magnetic energy of $(1.9 \pm 0.4) \times 10^{31}$ ergs, and the total positive and negative fluxes at the level of 0.01 $R_\odot$ are $(2.7 \pm 0.7) \times 10^{21}$ and $(-1.0 \pm 0.5) \times 10^{21}$ Mx, respectively. We notice that the total negative flux is much less than the total positive flux. This imbalance may be caused by the flaring emissions obscuring the dimming in the flare region, where the polarity is mainly negative. The obscured dimming is supposed to be at the footpoints of the calculated magnetic loops that link with the main dimmings (R1 and R2) dominated by the positive polarity.

TABLE 2

COEFFICIENTS OF THE SPEARMAN RANK CORRELATION FOR THE HEIGHT (H), SPHERICAL SEPARATION (D), AND LENGTH (L) OF THE CLOSED FIELD LINES CALCULATED IN TWO KINDS OF BOUNDARY CASES (SEE FIG. 3)

Conditions	ρ_H	ρ_D	ρ_L	N
$H \leq 0.2\ R_\odot$	0.94	0.91	0.91	1023
$H \leq 0.5\ R_\odot$	0.94	0.91	0.92	1310
$D \geq 0.2\ R_\odot$, $H \leq 0.2\ R_\odot$	0.73	0.73	0.69	189
$D \geq 0.2\ R_\odot$, $H \leq 0.5\ R_\odot$	0.76	0.72	0.66	260

NOTE.—N represents the sample number of the field lines satisfying a certain condition.

4.1.2. *SXR Transequatorial Loops*

The SXT observations show clearly the SXR transequatorial interconnecting loop (TIL) existing between AR 8210

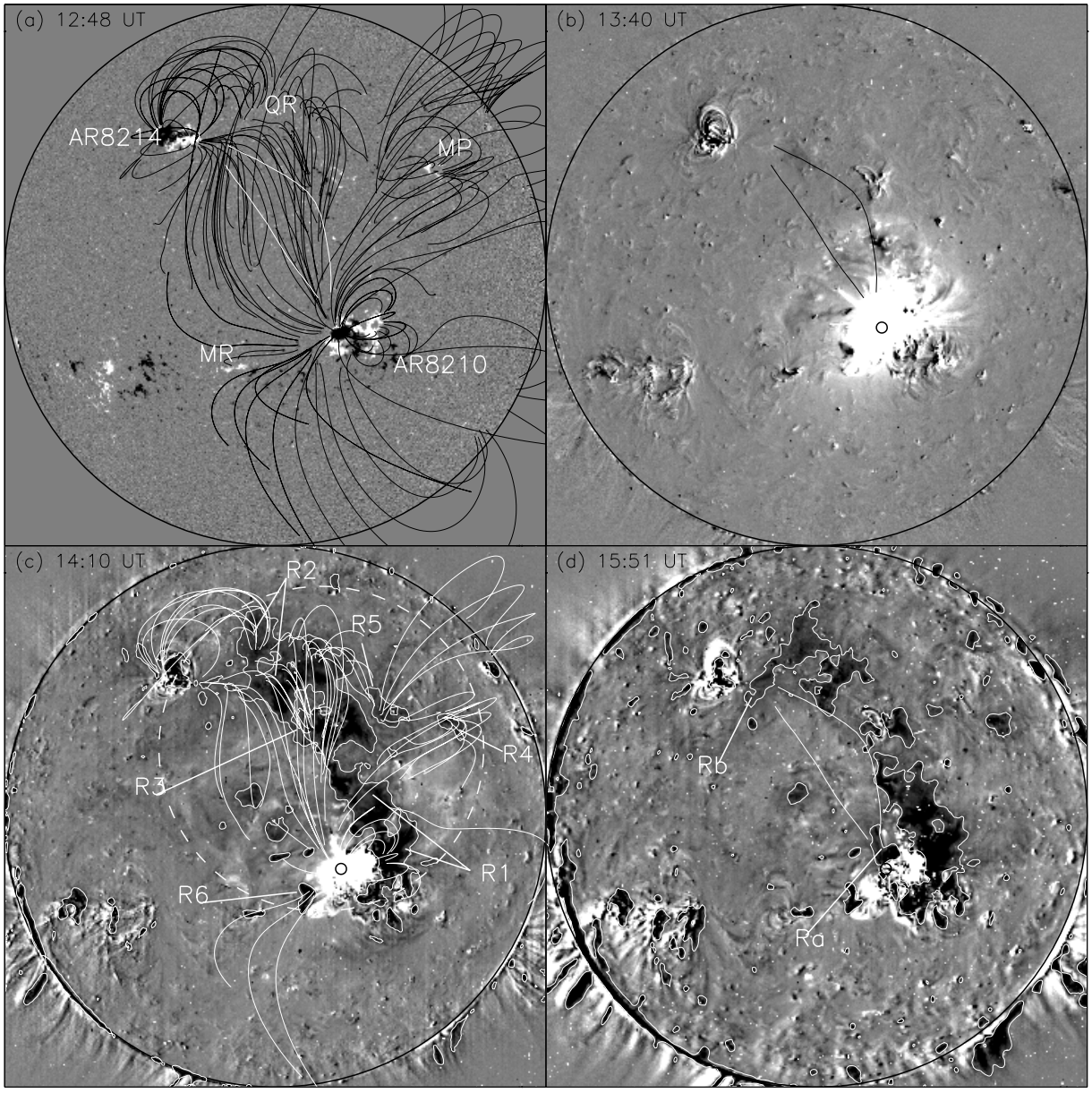

FIG. 4.—(*a*) *SOHO*/MDI magnetogram at 12:48 UT overlaid with the extrapolated field lines calculated from a global potential model. (*b*)–(*d*) EIT difference images, produced by referring to a preflare image at 13:20 UT. A small circle in panels (*b*)–(*d*) marks the site of initial flare brightening in SXR. In (*c*) the white contours demarcate the dimming regions with intensity decrease above the noise level of 3 σ; the white lines are those large-scale field lines that have one or two footpoints located at the dimming regions within a large white dashed circle.

and AR 8214 before the X1.1 flare (see Fig. 6*a*). For a comparison, we select some large-scale field lines that have one footpoint at AR 8210 and satisfy the conditions that heights are less than 0.5 $R_\odot$ and footpoint separations on the spherical surface are greater than 0.6 $R_\odot$. We find that these large-scale field lines can be grouped into four loop systems, denoted with L1, L2, L3, and L4, where L1 is related to the SXR TIL, L2 to the far extending EIT dimming R2, L3 to the MP, and L4 to the western limb. The parameters of these loop systems, including the average height, separation, and length, are listed in Table 3. We notice that the SXR TIL corresponds to the low field connectivity whose height is consistent with that for typical SXR loops ($H < 0.2\ R_\odot$; e.g., Švestka 1981). For the loop systems L2, L3, and L4, there are no SXR loop features corresponding to them, possibly because their heights are so high that their density and temperature are beyond a detectable range in SXT. The visibility of transequatorial magnetic connections is also related to the relevant heating mechanisms (e.g., Fárník, Karlický, & Švestka 1999; Pevtsov 2000).

We find that the SXR TIL disappeared or became dimmed after the flare, and distinctly some postflare loop-like features formed at the edge of AR 8210 where the preeruption TIL ended (see Fig. 6*b*). The EIT difference image showed no "deeper" dimmings appearing at the ends of the SXR TIL involved with its disappearance (see Fig. 4*c*), but a weak brightness decrease could actually be discerned in the nondifferenced images (see Fig. 1 in Thompson et al.

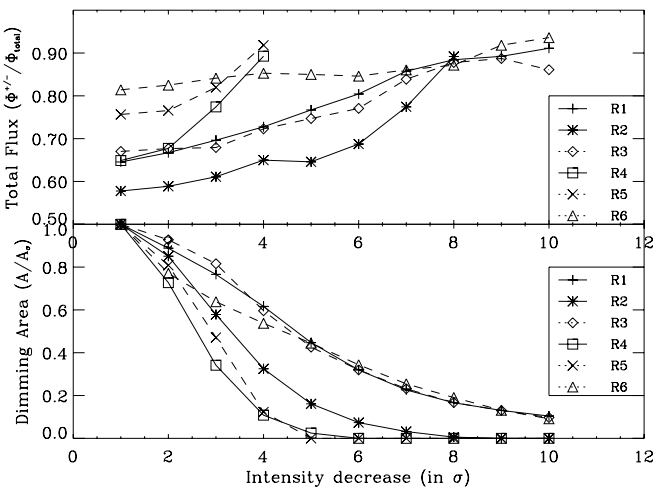

FIG. 5.—*Top:* Curves of magnetic flux of certain polarity ($\Phi^{+/-}$) over the total flux (Φ_{total}) in dimming regions with respect to the intensity decrease in units of σ, where σ is the noise level for the difference EIT image. *Bottom:* Curves of the normalized dimming area (A/A_σ) with respect to the intensity decrease, where A (A_σ) is the dimming area with intensity decrease above a certain value (1 σ). The solid lines represent that the dominated polarity of dimming regions is positive, and the dashed lines represent that the dominated polarity is negative.

2000). The dimming or disappearance of SXR TIL was very evident in the May 6, 8, and 9 eruptions (Khan & Hudson 2000).

We estimate mass and magnetic energy for the SXR TIL. The average electron density can be derived by using SXT filter ratios in the isothermal approximation (Tsuneta et al. 1991). We measured the temperature $T \sim 2$ MK and emission measure EM $\sim 4 \times 10^{47}$ cm^{-3} from the images Al.1/AlMg at 13:00 UT, for a transequatorial region with the length $D_1 = 5 \times 10^{10}$ cm and the width $D_2 = 1.8 \times 10^{10}$ cm (see the dashed box in Fig. 6*a*). Taking the loop height as $H \sim 0.2\ R_\odot = 1.4 \times 10^{10}$ cm, we derive the electron number density $N_e \sim 1.8 \times 10^8$ cm^{-3} and the mass value $M \sim 3.7 \times 10^{15}$ g for an emitting volume $V = D_1 D_2 H$. Using the same method as in § 4.1.1, we estimate the total magnetic energy $E_m \sim 1.1 \times 10^{30}$ ergs in a height range of 0.01–0.2 $R_\odot$ and the magnetic flux at the level of 0.01 $R_\odot$, $\Phi^+ = 1.0 \times 10^{21}$ Mx and $\Phi^- = 2.4 \times 10^{20}$ Mx. These preflare parameter values can be regarded as the maximum estimations of the contribution of the SXR TIL disappearance to the CME. We list the estimated quantities in Table 4.

4.2. *At the Flaring Active Region*

4.2.1. *Emission Features and the Bald Patch Topology*

During 12:00–16:00 UT on May 2, a BP in EIT and SXT was sustained at the south of AR 8210 and showed stability in position for 4 hr, with a displacement about 2.″5 northward and 5″ eastward. This BP corresponded to a bipole of magnetic elements in MDI magnetograms, so by taking this BP as a reference, the co-alignments of EIT, SXT, and MDI images for the flare region can be ensured in an accuracy of about 3″ (see Figs. 7*a*, 7*c*, and 7*d*). As this BP was not clearly visible in Hα, the Hα images were co-aligned with MDI or SXT by referring to full-disk images and correcting solar rotations for different time observations; in this way the co-alignment accuracy is about 5″.

In Figure 7*b*, the overlaid field lines are calculated in the same method as used for those shown in Figure 3*b*, but the footpoints of these field lines are extended to the height of 0.005 $R_\odot$ from 0.02 $R_\odot$ by employing a Gaussian quadrature scheme over 8×8 element subdivisions (Yan et al. 1993). Some low field loops between the central main magnetic structure and its northern positive polarities, which are not visible in Figure 3*b*, are also extrapolated. Moreover, our calculation meshes maintain the active region flux very well

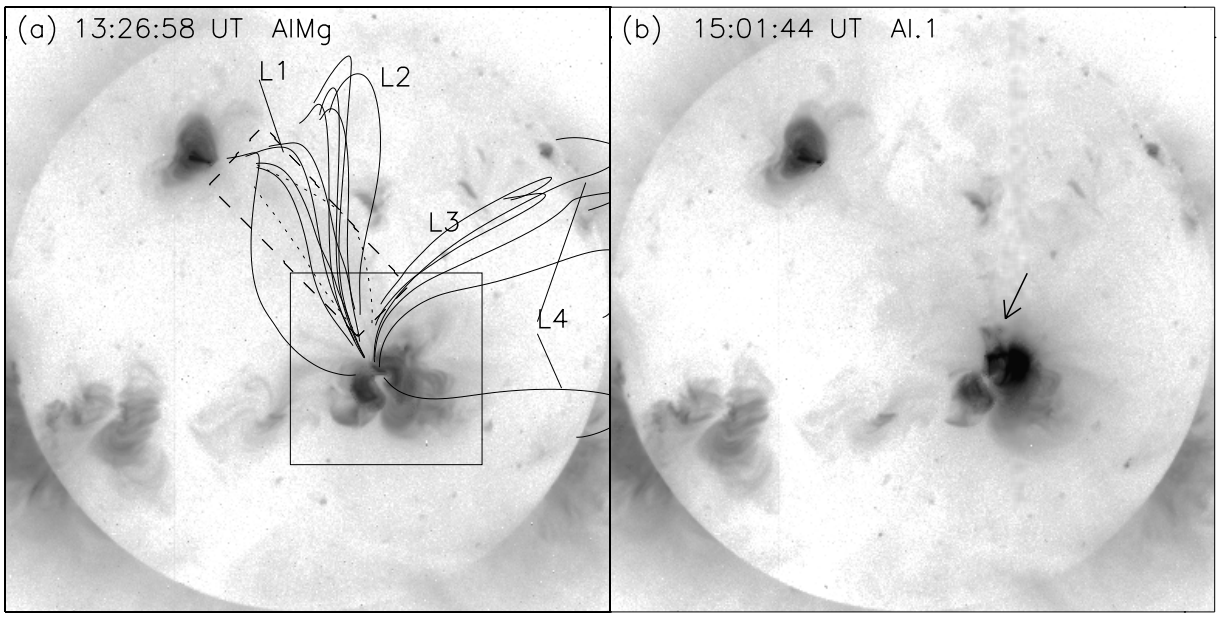

FIG. 6.—Comparison of the low coronal emissions between the images observed before and after an X1/3B flare by *Yohkoh*/SXT. (*a*) Overlay of extrapolated large-scale field line systems and the preflare SXR image at 13:26:58 UT; the dotted lines outline the SXR TIL. The region within the dashed-line rectangle is used to estimate the mass and magnetic energy of the plasma in the SXR TIL. The emission framed in a black box is shown in Fig. 7*a*. (*b*) Postflare SXR image at 15:01:44 UT. The arrow marks the looplike feature forming at the end of the preflare SXR TIL.

TABLE 3
PARAMETERS OF THE COMPUTED LARGE-SCALE FIELD LOOP SYSTEMS INCLUDING AVERAGE HEIGHT ($\bar{H}$), FOOTPOINT SEPARATION ($\bar{D}$), AND LENGTH ($\bar{L}$) IN UNITS OF SOLAR RADIUS

Loop Systems	$\bar{H}$	$\bar{D}$	$\bar{L}$
L1	0.15 ± 0.03	0.66 ± 0.04	0.82 ± 0.09
L2	0.32 ± 0.04	0.81 ± 0.06	1.27 ± 0.15
L3	0.26 ± 0.02	0.65 ± 0.01	1.07 ± 0.03
L4	0.31 ± 0.06	1.08 ± 0.10	1.70 ± 0.10

(see § 3.2), so their precision is good enough to allow us to approach the active region local topology. Figure 8 shows the presence of a "bald patch" (defined as the locations where the magnetic field is tangent to the photosphere) at the northern edge of AR 8210. Note that the bald patch is also a polarity inversion line, above which we obtain some field lines of a "dip" structure (not shown in Fig. 8). The calculated bald patch field lines do not show the connectivities with AR 8214 and the far extending dimming R2, but it does not exclude the possibility that the actual bald patch topology includes such magnetic connectivities because our calculations are based on the potential model, whereas the observed fields show the nonpotential at AR 8210 (see Fig. 10).

The *GOES* X-ray flux indicated the start of the X1.1 flare at 13:30 UT. In the preflare phase, a brightening feature (BF) appeared first at 13:27 UT in SXR (see Fig. 7*a*), which was associated with a newly emerging flux region (see § 4.2.2). Figure 7*a* shows that this brightening was located at the end of the SXR TIL. Figure 7*c* shows three straight bright loop features (e1, e2, and e3) in EIT at 13:20 UT, which well coincide with the SXR TIL in position. No EUV counterpart was seen corresponding to the SXR brightening at 13:20 UT; however, a curly filament (FL) was located near the BF (Fig. 7*c*); the FL was also seen in Hα (see Fig. 7*e*).

In the onset phase at 13:35 UT, an X-ray jetlike feature, J1, appeared at one end of the BF, directed to the SXR TIL (see Fig. 7*b*). North of the BF a "blob" emission developed into the other jetlike feature, J2, at about 13:36 UT and became much brighter than J1. The brightest SXR emission was at the center of the flaring brightening. These SXR features remained visible until 13:37:30 UT when *Yohkoh* entered nighttime. Figure 7*b* shows that both jetlike features are along the computed large-scale field loop systems (L1, L2, and L3 shown in Fig. 6*a*), and J2 is just coincided with the calculated bald patch (see Fig. 7*e*). The end positions of the EIT loops (e1, e2, and e3) imply that the calculated bald patch may extend to the footpoint of e1 actually, so it is also coincided with the end of J1. Figure 7*e* shows that in Hα the flare began at several bright kernels along the SXR flaring brightening. A weak bright Hα ribbon was seen coincident with the EIT loop e1 or the SXR jetlike feature J1; beside the bright ribbon, it was a dark surgelike feature in Hα that coincided with the footpoint of the EIT loop e2. Figure 9 shows evolutions of the SXR and Hα emissions just before an Hα ejection or hard X-ray (HXR) impulsive increase at about 13:38 UT. It is seen that in Hα a pair of bright kernels A and B on the sides of the magnetic neutral line corresponded to the footpoints of a compact SXR flaring loop, f1, while the kernels C and D corresponded to the footpoints of a longer SXR flaring loop, f2. In Hα, the brightenings increased and extended simultaneously, from kernel D toward the north to a "blob" and from kernel C toward the south around the central main spot, whereas in SXR the loop f2 manifested an expanding motion toward the northwest with an apparent speed of about 60 km s^{-1}, and its western end extended southward in agreement with the extending of kernel C in Hα.

The ejection happened at about 13:38 UT, which triggered a Moreton wave toward the northwest (Warmuth et al. 2000) and destroyed the "blob" in Hα. Instead, two flame-shape features, h1 and h2, appeared at the end of the preflare SXR TIL (see Fig. 7*f*); h1 was stationary, while h2 moved toward h1. They merged into a brighter elongation at 13:40 UT and then decayed rapidly. It is worth noticing that the curly filament beside the brightening C remained visible during this ejection (see Figs. 7*f* and 9*d*–9*f*); this filament was also confirmed as nonerupting in EIT, which was clearly visible after the postflare emissions decayed. Hence, this ejection was not involved in the filament eruption. The emission features such as the preflare sheared SXR loops (f1 and f2 seen in Figs. 9*a*–9*c*) and the postflare potential-like arcades (seen in Fig. 7*d*) in addition to the magnetic features (see § 4.2.2) suggest that the flare ejection may correspond to the eruption of a twisted emerging flux system.

4.2.2. *Magnetic Evolution Features*

The magnetic structure of AR 8210 is characterized by a large negative polarity of apparent clockwise rotation surrounded with a sequence of small emerging positive flux. The rotation feature of the main spot was also clearly visible in the white light (Warmuth et al. 2000). The southern emerging positive flux region (see Fig. 7*a*) produced a series of flares and associated CMEs on May 1 and 2 (Sterling & Moore 2001), while the northern emerging positive flux region was responsible for an X1/3B flare on May 2.

Figure 10 shows the evolution of Huairou vector magnetograms on May 2. The MDI 90 minute cadence movie indicates that the N1, including N1a, N1b, and N1c, was an older magnetic structure in connection with the main polarity S1, decaying on May 2. The rapid decrease of its total flux during 12–20 UT (see Fig. 11) was due to the disappearance of N1c. Magnetic structure, N2 and S2, was born at about 12 UT on May 1. The bipoles N2a and S2a first emerged and S2a moved westward away from N2a, then the other bipoles N2b and S2b emerged at about 04 UT on May 2; N2b moved eastward and linked with N2a, while S2b moved westward and merged into S2a. The field connections between N2 and S2 were well indicated by the alignments of the transverse field (see Fig. 10*b*), which were also evidenced by the pronounced arch filament systems (AFSs) in Hα (Warmuth et al. 2000). The rapid increases of total flux for N2 and S2 from 04 to 10 UT (see Fig. 11) correspond to the emergence of the bipoles N2b and S2b. The average speed of motion of S2 was about 390 m s^{-1}.

The most important magnetic structure for the flare trigger was found to be a newly emerging sheared flux system, N3 and S3. N3 was born at about 23 UT on May 1 and moved toward the southeast at a speed of about 140 m s^{-1}; at 19 UT on May 2 it merged with N1c, then intruded into the main polarity S1 (see Fig. 10*d*). The negative counterpart of N3 is not easy to discern, but the alignment pattern of the transverse field suggests that N3 connected with the neighbor region S3. The bipoles N3 and S3 coincided with

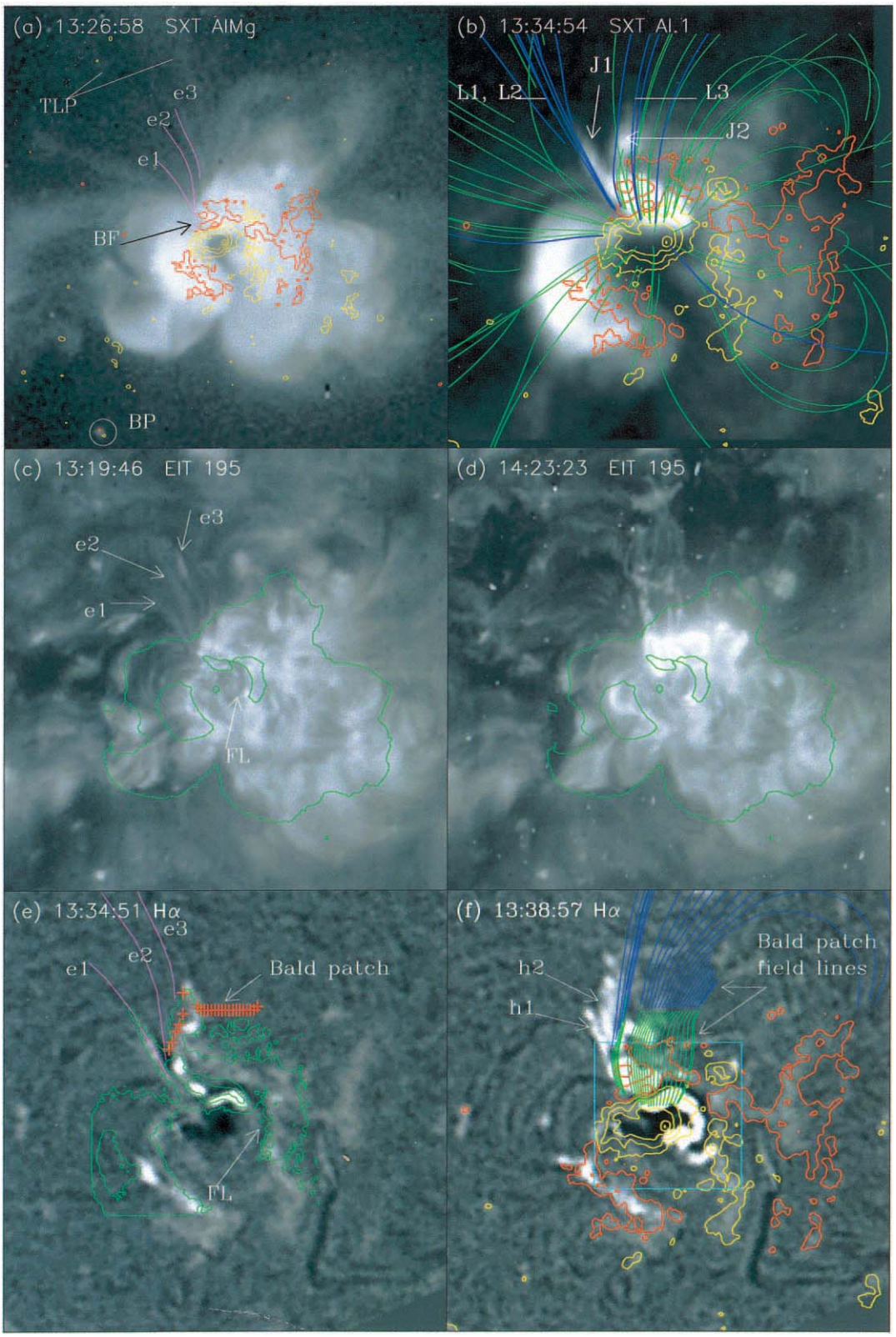

FIG. 7.—Comparisons of multiwavelength emissions and the magnetic field at the flaring active region AR 8210. (*a*) SXT image overlaid with the MDI magnetogram at 12:48 UT in contours, with the red color representing positive polarity and the yellow color representing negative polarity; the levels are ±100, 500, and 1000 G. The purple lines indicate positions of the EIT loops marked in (*c*). A small white circle in the bottom left corner marks a bright point corresponding with a pair of magnetic elements in position; by referring to this feature the co-alignments among SXT, EIT, and MDI images can be improved to an accuracy of about 3″. (*b*) SXR image overlaid with the same magnetogram in contours as in (*a*). The green or blue lines represent the calculated field lines based on a global potential model; particularly, those large-scale field lines (see Fig. 6*a*) are underlined in the blue color. (*c*) and (*d*) EIT images overlaid with contours of the SXR emission shown in (*a*). (*e*) Hα image overlaid with contours of the SXR emission at 13:35:20 UT. The purple lines have the same meaning as in (*a*). The red crosses show the calculated bald patch. (*f*) Hα image overlaid with contours of the same MDI magnetogram as in (*a*). The green or blue lines are the calculated bald patch field lines. A light-blue box marks the region where the magnetic evolution is shown in Fig. 10. The field of view for (*a*), (*c*), and (*d*) is 604″ × 604″, while the field of view for (*b*), (*e*), and (*f*) is 302″ × 302″. (Error correction: label "TLP" in (*a*) should be "TIL.")

TABLE 4
DERIVED PARAMETERS FOR EIT DIMMINGS AND THE SXR TIL

Surface Features	M ($\times 10^{15}$ g)	E_m ($\times 10^{31}$ ergs)	Φ^+ ($\times 10^{21}$ Mx)	Φ^- ($\times 10^{21}$ Mx)	A ($\times 10^{21}$ cm^2)	N_e ($\times 10^8$ cm^{-3})
Dimmings[a]	11 ± 7	1.9 ± 0.4	2.7 ± 0.7	1.0 ± 0.5	1.2 ± 0.8	~ 4
[b]	5.7 ± 3.8	...	...	...	...	~ 2
SXR TIL[c]	3.7	0.11	1.0	0.24	0.9	1.8

NOTE.—M, E_m, $\Phi^{+/-}$, A, and N_e are mass, magnetic energy, positive/negative flux, area, and electron number density, respectively (see § 4.1).
[a] N_e is the mean value for the data ranging from 0.01 to 0.2 $R_\odot$ in the model of Zheleznyakov 1970.
[b] N_e has the same meaning as in footnote a, but for the data in Allen's models (Arthur 2000).
[c] N_e is derived from SXT filer ratios (Tsuneta et al. 1991).

the compact flaring loop f1 in SXR (Fig. 10*c*). S3 is likely a branch of the main polarity S1. Figures 10*a* and 10*b* show that the strong magnetic shear developed along the neutral line as N3 emerged, while it appeared very relaxed after the flare (Fig. 10*d*). Figure 11 shows that the total flux of N3 linearly increased at an emerging rate of about 7.4×10^{15} Mx s^{-1} until the flare occurrence and then decreased by about 4.1×10^{19} Mx during 12:48–14:24, which amounts to 4.7×10^{29} ergs considering a layer of 1 Mm thick; afterward N3 slowly decayed in total flux.

In addition, we notice that the main polarity S1 continued to grow on May 2; its total flux increased from 8.6×10^{21} to 9.7×10^{21} Mx with an average emerging rate of about 1.2×10^{16} Mx s^{-1} (see Fig. 11). On the other hand, from the observed transverse fields, we measure the average shear or twist for the whole region to be $\alpha = (3.7 \pm 0.5) \times 10^{-8}$ m^{-1} by using a linear force-free field fit (Wang & Abramenko 2000), which was stronger compared with typical sheared active regions for which 0.8×10^{-8} m$^{-1} \leq |\alpha| \leq 1.9 \times 10^{-8}$ m^{-1} (Aulanier et al. 1998). Thus, the apparent clockwise rotation of the main spot S1 may correspond to the emergence of a strong twisted flux tube, which thus can supply a large amount of free magnetic energy for producing a series of flares in this active region.

5. DISCUSSION

5.1. *Summary of the Results*

We have studied a halo CME that occurred on 1998 May 2, which was associated with an X1/3B flare occurring at 13:42 UT in AR 8210. We reconstruct its large-scale coronal field structure from a composite boundary of the MDI full-disk magnetogram and Kitt Peak synoptic maps based on a global potential model. The extrapolated large-scale field lines can well model the SXT transequatorial loop and interpret the widely extending EIT dimmings. The coordinated diagnoses of emission features in Hα, EUV, and SXR and magnetic features in topology and evolution for the source region provide the evidence for this CME initiation resulting from the interaction between the large-scale loop systems and a rapidly emerging twisted flux system by magnetic reconnection, for which a scenario is proposed to interpret this event in § 5.5. We first summarize our obtained results as follows.

Calculations of the field lines indicate that widespread large-scale loop systems and some open field lines are linked with the source region AR 8210, which has a distinct flux imbalance between the positive and negative polarities. EIT observations show that dimmings were located on a very

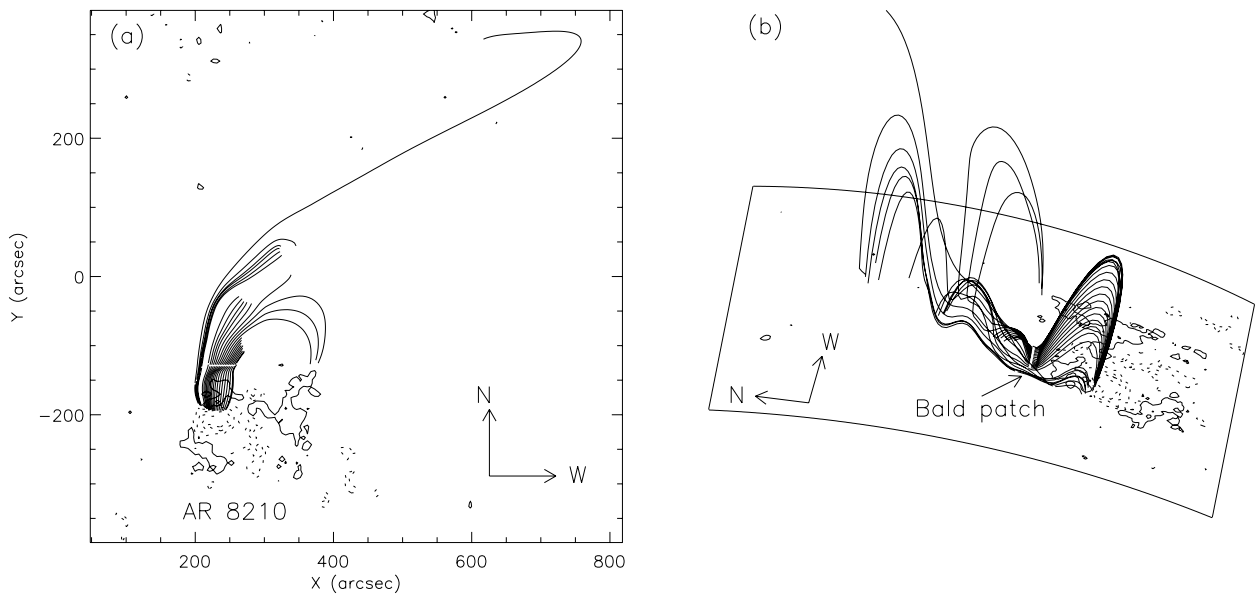

FIG. 8.—(*a*) Projection from the top of the computed bald patch field lines that form the separatrix. The origin of the Cartesian coordinates is set at the disk center. (*b*) Perspective view of the same field lines. A factor times 10 radial stretching is applied in order to get a better view of these very flat field lines.

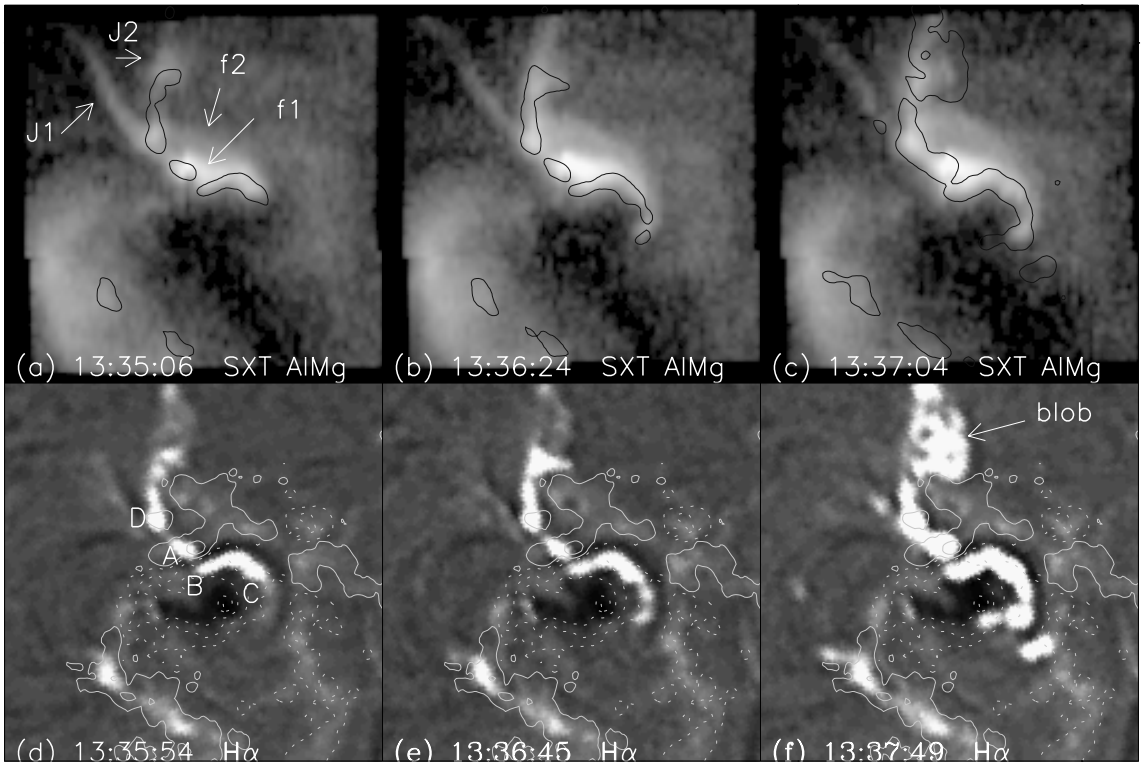

FIG. 9.—(*a*)–(*c*) SXT images overlaid with the contours of Hα bright kernels shown in (*d*)–(*f*). (*d*)–(*f*) Hα images overlaid with the contours of the MDI magnetogram at 12:48 UT; the contour levels are the same as in Fig. 7*a*.

large scale, extending from AR 8210 to the opposite hemisphere regions near AR 8214; the dimmings closer to the flaring region underwent an intensity decrease more seriously. We find that the major dimmings are located at footpoint regions of the field loops linking with the flaring region, whereas some dimmings are not directly related to the flaring region, but they are linked with those immediately flare-related dimmings. The unipolar feature of dimmings is also confirmed by the distinct flux imbalance at these regions. We find that an SXR TIL well coincides with the low large-scale field line system with a height of about 0.15 $R_{\odot}$ and that this SXR TIL disappeared after the flare; however, the substantial EIT dimmings were not observed at its footpoints but were located on its one side. Estimates of mass, magnetic energy, and flux for the ejected plasma from the EIT dimming regions are comparable to the output of a large CME.

At the CME source region (AR 8210), we notice that the flare began as the appearance of a looplike brightening near the end of the SXR TIL, and then two jet features rapidly developed at the edge of this brightening toward the TILs, and their ends coincide well with the calculated bald patch. Co-alignments of Hα and short-exposure SXT images identify that the initial brightening was composed of two loops, a brighter compact one overlaid by the other longer one. The jets were located at one end of that longer loop, which manifested an expanding motion with an apparent speed of about 60 km s^{-1} just before the impulsive HXR increase. After an ejection observed in Hα, two flame-shape brightenings appeared at the end of the preflare SXR TIL. The Hα and EIT observations showed that this flare was not associated with eruption of the filament, which was identified as still remaining after the flare. Magnetic evolutions showed that the X-ray jet-related longer flaring loop was associated with a slowly decaying structure, while the underlying brighter compact one was associated with a newly emerging twisted flux region (EFR). The total flux of this EFR kept increasing at a rate of 7.4×10^{15} Mx s^{-1} before the flare, accompanied by the development of strong shear along the magnetic neutral line; after the flare its total flux decreased by 4.1×10^{19} Mx, while the strong shear was relaxed very much.

The filament around the main spot is observed without eruption in the flare, although it is very close to the flare-related EFR. This may be explained by the fact that the topological change of the active region for the flare (likely the opening of the EFR system) did not lead to an equilibrium loss of the neighbor field system binding the filament. Recall that the Hα brightening developed and extended only on the inside of the curly filament as the overlying sheared SXR loop rapidly expanded (see f2 in Fig. 9). This implies that the overlying flux of the EFR, which is supposed to be opened in the flare, did not bind or bound only a very small part of the filament in the preflare phase, whereas the filament could be mainly confined by strong magnetic loops at the west of the active region (see Fig. 7*b*).

5.2. *Magnetic Energy Buildup and Release*

Some studies of the observed vector magnetic fields have showed evidence for the emergence of current-carrying (or twisted) flux tubes (Wang et al. 1994; Leka et al. 1996; Wang & Abramenko 2000). In this way, active regions can build up the free magnetic energy in the atmosphere to power flares. Our measurements of the magnetic flux and the twist α suggest that the central main spot is such a large emerging

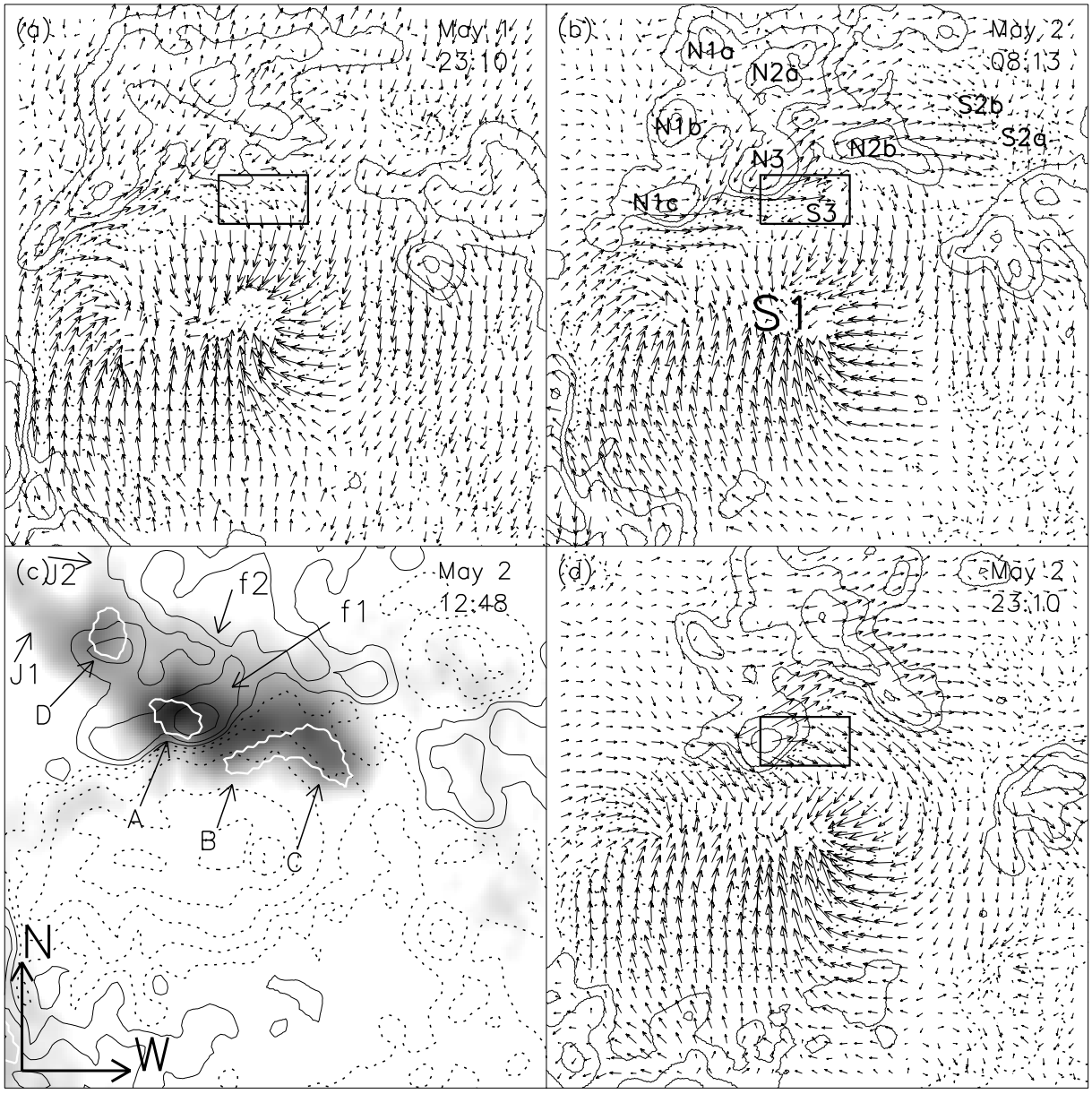

FIG. 10.—Evolution of the photospheric magnetic fields in AR 8210. (*a*), (*b*), and (*d*) Huairou vector magnetograms. For the regions framed with a small black box in (*a*), (*b*), and (*d*), the twist $\alpha = 0.069$, 0.74, and 0.10 Mm^{-1} are measured, respectively, by a force-free field fit to the observed transverse field. (*c*) MDI magnetogram overlaid with the SXR emission (*gray*) at 13:35:06 UT and with Hα bright kernels (*white contours*) at 13:34:51 UT. The thin contours in all figures demonstrate the intensity of the longitudinal field (levels of $\pm$50, 200, 500, 1000, and 1500 G); solid lines show the positive field, and dashed lines show the negative field. The short arrows indicate the transverse field. The field of view for all figures is $100'' \times 100''$.

flux tube of strong twist. We notice that the sense of its twist is right-handed ($\alpha > 0$), so if we assume that this large flux tube is fragmented into some branches at the periphery, which coil the main trunk in a helical shape (Ishii, Kurokawa, & Takeuchi 1998), then the intersections of the flux tube on the photosphere manifest a clockwise rotation as it rises. Actually, such a feature was markedly observed throughout the development of the main spot (Warmuth et al. 2000). On this assumption, the rising speed of the flux tube can be estimated by

$$v_{\mathrm{rise}} = \frac{\omega}{q} , \tag{12}$$

where $q \equiv d\phi/dl \approx \alpha/2$ is the twist per unit length and $\omega = d\phi/dt$ is the angular velocity of the spot rotation. The $\alpha \approx 4.2 \times 10^{-8}$ m^{-1} is measured for the main spot by a linear force-free field fitted to the observed transverse field (Wang & Abramenko 2000), and $\omega \approx 5^{\circ}$–15° day^{-1} is taken from Warmuth et al. (2000); we then obtain $v_{\mathrm{rise}} \approx 48$–$144$ m s^{-1}. The emergence of an inherently twisted structure may produce the vortical flow near the surface because cold, dense plasmas carried by the rising flux tube will slide down along the helical field lines. In our case, the rising flux tube has the right-handed twist, so it produces the clockwise vortical flow. The speed of the vortical flow is

$$v_{\mathrm{flow}} = (v_{\mathrm{rise}} - v_p) q R , \tag{13}$$

where v_p is the rising speed of the carried plasmas and R is

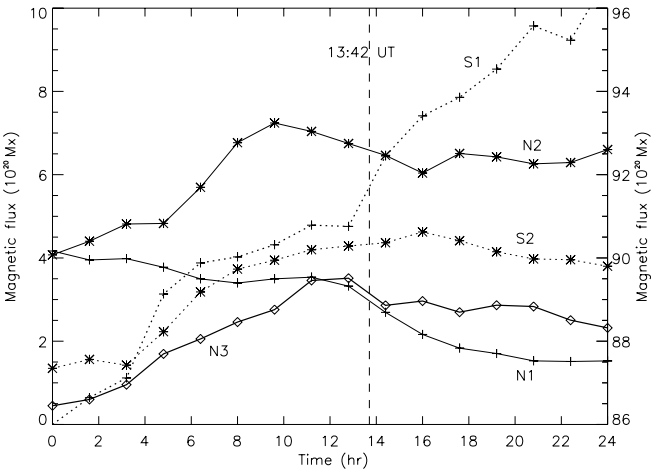

FIG. 11.—Temporal variations of the total flux of magnetic polarities in AR 8210 during May 2. Particularly, the flux curve for the main polarity, S1, is measured with the right y-axis coordinates. The cutoff for measurements of the total flux is 150 G. The solid curves are for the positive polarities, and the dashed curves are for the negative polarities.

the radius of the flux tube. When $v_p = 0$, it implies that the contained plasmas in the flux tube do not rise following the field lines, so we obtain the maximum vortical speed $v_{\rm flow} = v_{\rm rise} qR = \omega R \approx 22$–66 m s^{-1}, where $R \approx 22$ Mm is the radius of the main spot. Thus, to distinguish the spot rotation produced by the emergence of the twisted flux tube from that by surface vortical flows is generally difficult, requiring a systematic comparison between observations and models.

On May 2, except for the large X-class flare we studied, there were no other major flares occurring in AR 8210. Hence, the development and relaxation of strong shear near N3 could be related to the accumulation and release of the free magnetic energy responsible for this flare, although the Huairou vector field data did not cover just the flare time. During the preflare period ($\sim$14 hr), the total flux of EFR N3 increased to about 3.5×10^{20} Mx from 0.5×10^{20} Mx, while the twist α increased to $\sim$0.74 Mm^{-1} from $\sim$0.069 Mm^{-1} within 9 hr; after the flare α reduced to $\sim$0.10 Mm^{-1} (see Fig. 10). For the bipole N3S3, we estimate its free magnetic energy by

$$E_{\rm free} = \frac{1}{2} LI^2 , \qquad (14)$$

where $I = \alpha\Phi/\mu_0$ is the coronal electric current on a force-free field assumption and $L \approx l\mu_0/4\pi$ is the self-inductance where l is the length of the coronal flux tube, which is taken to be a semitoroid. We measure the footpoint separation $d \approx 11$ Mm and thus obtain $L = 1.7$ H. Taking $\Phi = 3.5 \times 10^{20}$ Mx, we obtain $E = 3.1 \times 10^{29}$, 3.6×10^{31}, and 6.6×10^{29} ergs for the cases $\alpha = 0.069$, 0.74, and 0.10 Mm^{-1}, respectively. Thus, the free magnetic energies possibly accumulated and released for the EFR system N3S3 are approximately several times 10^{31} ergs, consistent with the typical energy for X-class flares (Švestka 1981). Studies of active region fields suggest that the free energy does not generally exceed one-third of the total magnetic energy (e.g., Klimchuk & Sturrock 1992). For examining the validity of the estimated free energy, we estimate the total field energy of the bipole N3S3 assuming a cylindrical flux tube with constant magnetic field (Vourlidas et al. 2000),

$$E = \frac{1}{8\pi} \int_{\rm flux\ tube} B^2\, dV \approx \frac{1}{8\pi} \frac{l}{A} \Phi^2 , \qquad (15)$$

where l is the length of the flux tube and A is the area of the flux tube. Taking $A \approx 30$ Mm^2 for the area of N3, we obtain $E = 2.8 \times 10^{31}$ ergs. Hence, the available free energy stored in N3S3 is $E_{\rm free} \leq E/3 \approx 1 \times 10^{31}$ ergs. This energy limitation corresponds to a twist $\alpha \approx 0.4$ Mm^{-1} calculated by equation (14), which is in good agreement with average values of α for EFR bipoles in Leka et al. (1996). Considering that a portion of free energy could be stored in the preexisting overlying fields, the estimated value of the free energy for the EFR system is reasonable.

Recall that the bipole N3S3 also manifested a shearing proper motion with the velocity $v_{\rm sh} \approx 140$ m s^{-1} in the preflare phase, and this motion still remained in the postflare phase (see Fig. 10). Such proper motions can also produce the shear or build up the free magnetic energy (Klimchuk & Sturrock 1992). As a simple estimate, approximating the coronal field of the bipole by a cylindrical flux tube and assuming that the footpoints are prevented from rotating as the bipole is sheared, the angle of twist $\delta\phi$ is (Leka et al. 1996)

$$\delta\phi = 2 \tan^{-1} \left(\frac{v_{\rm sh}\tau}{d/2} \right) , \qquad (16)$$

where τ is a time for which the shearing motion $v_{\rm sh}$ is applied and d is the initial distance between the footpoints. Taking $d = 11$ Mm and $\tau = 10$ hr, we obtain $\alpha \approx 2q = 2\delta\phi/l = 0.17$ Mm^{-1}, where l is the length of the flux tube taken to be a semitoroid. By using equation (14), the free energy resulting from the shearing motion is calculated as $E \approx 2 \times 10^{30}$ ergs. This value suggests that the shearing motion could not produce the sufficient energy for powering the X-class flare but may explain the observed twist ($\sim$0.10 Mm^{-1}) measured 10 hr after the flare (see Fig. 10*d*), which shows an agreement with the generated twist.

5.3. *Boundary Element Method for a Global Field Extrapolation*

We have first applied the BEM (Yan et al. 1993) to solve the solar global field problem based on a potential assumption. Different from the spherical harmonic expansion method (Newkirk et al. 1968) and the GFM (Sakurai 1982), the BEM takes numerical meshes to fit the boundary and thus transforms solving a boundary integral problem into solving a linear problem. Although the GFM also belongs to the integral technique, it searches for an obvious integral solution representation in light of the special boundary symmetry, so it is generally very difficult. In the application of the BEM for an infinity boundary case, we first determine distributions of the potential on the boundary by solving a linear equation group in order to obtain the potential at any interior point. Actually, this step is not necessary because the exact solution can be expressed in the integral form by using the GFM (Kellogg 1953). However, in the case of the source boundary problem for modeling the solar wind effect, the GFM can only give an approximate solution (Sakurai 1982), while the BEM can be applied in a similar way as used in the former case. Moreover, because there are no requirements on the shape of the boundary, the BEM

can allow us to specify an irregular source boundary that may meet the feature that the coronal fields at different regions become radial actually at different height levels. The main difficulty for the BEM is that, to acquire a high resolution of boundary meshes, we need to solve a huge set of linear equations, which may be limited by present capabilities of computers.

The validity of the extrapolation presented in this study may arguably be attributed to some approximations. We took the infinite boundary and removed the polar regions because of numerical mesh constraints. However, the total fluxes of the polar fields were of the same order as those in the equatorial zone on the radial field assumption and so are not negligible. The source surface method with the radial field assumption yields the large open field regions at high latitudes, showing good agreement with the observed polar holes, which typically extend down to a latitude of $\sim 60^\circ$ near sunspot minimum (Wang & Sheeley 1992). This implies that the polar fields are somehow very weakly related to the active region fields, and the source surface condition plays a significant role in successfully modeling this open field feature. While in the infinite boundary case, an approximate test shows that the inferred polar fields by the radial field correction yield magnetic connections with the active regions, showing disagreement with observations. In this sense the removal of the polar fields is consistent with the choice of the infinite boundary, which may be a good approximation for the modeling of magnetic connections in low latitudes. In addition, some independent studies found that transequatorial loops predicted by Cartesian extrapolations from a central disk magnetogram are present in coronal observations (Fárník et al. 1999; Delannée & Aulanier 1999), demonstrating that the neglect of the polar fields is a reasonable approximation. Another approximation is that we regarded the observed line-of-sight fields as the radial components required by the boundary condition because the radial field assumption is obviously invalid for active regions. This approximation is reasonable since the major active regions, AR 8210 (S15°, W15°) and AR 8214 (N25°, E25°), are located near the disk center. The disparity caused by the projection effect is very small.

5.4. *Surface Signatures of a Halo CME and Its Output*

The CME from 1998 May 2 is a good example of "halo" CMEs, typical of eruptions that occur near the solar disk center. We have studied its large-scale low coronal field structure and associated surface signatures. We find that EIT dimmings extended over a great deal of the solar disk with a slow decay for several hours and were mostly located on the footpoints of the extrapolated field loop systems, indicating that these dimmings are most likely due to density depletions via an expansion or ejection of the flare-related loop systems (Hudson et al. 1996). This result is consistent with that in Delannée & Aulanier (1999), who studied a case of the similar north-and-south active region geometry. One difference is that in their case EIT dimmings were located between the two major active regions, associated with the TIL, while in the present case dimmings deviated from the SXR TIL. This feature can be explained by our field extrapolations, which show several large-scale loop systems linking with the flaring active region; one is coincident with the SXT TIL, while another connects the far extending dimmings. Therefore, we conjecture that the main component of this CME, seen at the northwest limb in LASCO/C2 (Fig. 1*b*), is contributed by the opening of the dimming-related loop system, while the SXR TIL-related field system is only partially opened in the CME, thus causing weak dimmings at its ends.

The other new feature we find is that some dimmings are not directly related to the flaring region by field connections, but they are linked with those immediately flare-related dimmings. This feature may be explained by a global restructuring resulting from successive interaction of the multipolar magnetic systems (Pick et al. 1999b). The large-scale magnetic restructuring may also lead to eruption of the loop system that linked the far extending dimming and AR 8214 (see Fig. 4*a*), contributing to the northeast component of the CME (see Fig. 1*b*). In addition, the field extrapolations show that the SXR TIL corresponds to the low field connectivity ($H \sim 0.15\ R_\odot$), while the far dimming-related loop system belongs to the high connectivity ($H \sim 0.32\ R_\odot$). The latter was not seen in SXR, probably as a result of its density and temperature beyond a detectable range for SXT.

It is known that basic quantities of the CMEs such as mass, velocity, and geometry can be computed from the measurement of the limb events (e.g., detected by LASCO), and in some special cases the potential, kinetic, and magnetic energies also can be derived (Howard et al. 1985; Vourlidas et al. 2000). The measurements of these quantities are very important for the study of driving forces in CMEs and space weather effects. However, for halo CMEs (the Earth-directed CMEs) such measurements become invalid; the only way is to make use of various indirect indicators of CMEs on the disk, for example, SXR dimmings (Sterling & Hudson 1997). In this study, via the low coronal features such as the EIT dimming and the dimmed SXR TIL near the launching of a halo CME event, we estimate the mass, magnetic energy, and magnetic flux of the ejected plasma. The obtained values of mass and magnetic energy are comparable with those derived from the limb events, and the total flux has the same order of magnitude as the average flux [$(1.3 \pm 1.1) \times 10^{21}$ Mx] of several magnetic clouds observed by *Wind*, which occurred at the same time interval as the LASCO CMEs (1997–1998; Vourlidas et al. 2000).

The validity of the mass and magnetic energy estimations for the CME may be questioned for several reasons. Firstly, we did not take into account the geometry of the calculated loops, i.e., the calculated three-dimensional volume in which field lines have their footpoints in the dimmings; this is because not all dimmings exactly correspond with the footpoints of the calculated loops. However, a large part of the CME mass could come from the dimming regions, as the electron density in the body of the coronal loops is lower. Secondly, we assume that the preflare plasma contained in the dimming regions is completely depleted for the CME mass, which may lead to an overestimation. Finally, the estimates from the SXR TIL should be regarded as the maximum contributions to the CME because the weaker dimmings at its ends suggest that the SXR TIL seemed to only partially disappear or be opened.

5.5. *Interpretation of the Flare CME Event*

Our results obtained from the analyses of emission features and magnetic evolutions at the source region AR 8210 suggest that the interaction between the large-scale loop sys-

tems and a newly emerging twisted flux system leads to the eruption of an X-class impulsive flare and the subsequent large-scale restructuring responsible for a halo CME. We propose a scenario, sketched in Figure 12, that can reproduce many observed features as follows.

Preflare evolution.—A new twisted flux system (N3S3) emerges around the main spot, pushing up the overlaying preexisting field system (N1S1) and continuously accumulating magnetic free energy in the systems, as evidenced by developments of strong shear along the neutral line. The emerging motion drives a slow reconnection at a bald patch at the north of AR 8210. This reconnection converts the overlaying flux from small active region connections to the large-scale transequatorial connections and meanwhile heats the chromospheric plasmas evaporated into the coronal loop systems formed by the separatrix field lines. The preheating process can explain the brightenings appearing in EIT (such as e1, e2, and e3) and in SXT (such as TIL and BF; see Fig. 7) before a flux rise of the *GOES* SXR. In the rising phase, the SXT observations show the jetlike features at the places of the calculated bald patch. This is strong evidence for the bald patch reconnection, similar in topology and mechanism to the reconnection models for explaining the chromospheric jets at sites of emerging flux (Yokoyama & Shibata 1995). However, it is worth pointing out that the general X-ray jets are associated with small flares (e.g., Shibata, Yokoyama, & Shimojo 1996), while in our case the jetlike features appear at the rise phase of an X-class flare. In addition, at this phase the radio observations show that the starts of several type III bursts are directed to the north of AR 8210, and the radio emissions follow the SXR transequatorial loop (Pohjolainen et al. 1999, 2001). These radio bursts are excited by propagation of the electron beams along the field lines, which are likely produced by the bald patch reconnection.

Flare evolution.—The slow reconnection at the bald patch continues to reduce the overlaying fields above the twisted EFR flux until a critical point is reached when the confined inner flux system can erupt explosively outward. The SXT observations indicate a fast expanding motion of the overlaying loops above a bright core, several minutes before an ejection in Hα. This fast outward motion may be a precursor of the flux eruption. At 13:37:30 UT, almost simultaneously with the Hα ejection, an impulsive, very large increase in the radio and hard X-ray emission takes place, and the radio flux shows an increase toward the high frequencies (Pohjolainen et al. 2001). These features are caused by the drastic energy release according to the standard flare model (fast reconnection in the induced current sheet) as the eruption begins. Such plasmoid-induced reconnection has been strongly evidenced by the X-ray hot plasma ejection in impulsive flares (Shibata et al. 1995; Ohyama & Shibata 1998). This fast reconnection also produces the postflare loops (seen in EIT) and two flare ribbons at the footpoints (seen in Hα). Most energy released in the flare may be extracted from the twisted EFR system. The flare leads the shear relaxation and flux decay (or decrease). The eruption may also lead to the current sheet forming at the bald patch, so the fast reconnection produces the brightenings in Hα such as h1, h2, and "blob" (see Figs. 7*f* and 9*f*). The erupting sheared core expands and pushes upward the large overlaying loop opening, which may interact with other magnetic systems in the path of its expansion to lead to a global restructuring responsible for an explosive halo CME. The coronal fast shock generated in the flare, suggested by the Moreton wave (Uchida, Altschuler, & Newkirk 1973), may also play a role in pushing up the large loop systems to open and interact with other systems. The EIT dimmings are expected to be at the footpoints of the opening field regions.

Our scenario for a flare CME is similar to the "magnetic breakout" model (Antiochos 1998; Antiochos et al. 1999), in principle, but different in the topological geometry. In the breakout model, a slow reconnection to remove the overlying flux above the sheared core takes place at a null point high in the corona. Aulanier et al. (2000) observed a flare in a multipolar, delta-spot region with a null point. Using the Transition Region and Coronal Explorer (TRACE) data,

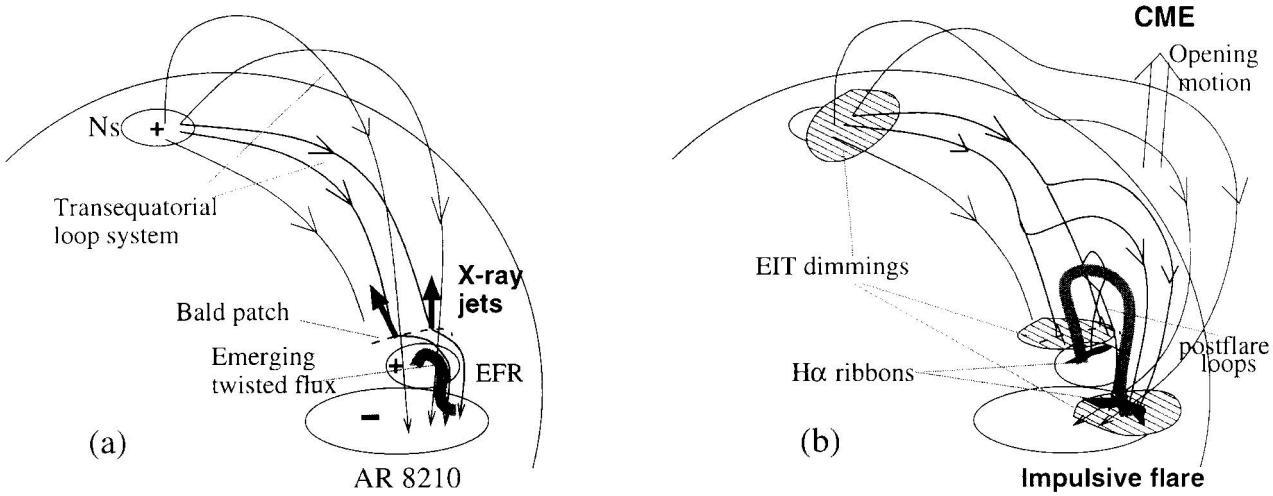

FIG. 12.—Sketch of the scenario for a flare CME initiation. (*a*) Newly emerging twisted flux system (EFS) pushes up the overlying preexisting flux system (PFS) in AR 8210, accumulating the free magnetic energy. The expanding motion drives a slow reconnection at a bald patch between PFS and the transequatorial loop system (TLS) producing X-ray jets and lighting up the involved coronal fields. "Ns" represents the positive polarities in AR 8214, QR, and MP (see Fig. 4*a*). (*b*) Reconnection at the bald patch removes the overlying flux and leads to an explosive eruption of the confined EFS, producing an impulsive flare and postflare loops via the standard model. The energetic erupting flux pushes upward the large-scale TLS to expand or open, producing a CME. The dimmings form at the footpoints of the opening field lines. [*See the electronic edition of the Journal for a color version of this figure.*]

they detect slow preflare motions of loops in EUV beginning more than an hour prior to flare maximum and suggest that this is an indicator of the breakout reconnection at the null point. While in our case there is no null point existing, the field extrapolations instead reveal the presence of a bald patch near the edge of an EFR. The slow reconnection at the bald patch (without the vertical current sheet formation) is suggested by the features such as preflare loop brightenings in EUV and X-ray jets occurring in this place. The low-cadence EIT observations do not allow an exploration of such preflare motions of the EUV loops for a direct comparison with those seen by Aulanier et al. (2000) in TRACE.

Delannée & Aulanier (1999) also observed a flare near a parasitic polarity region with a bald patch topology. They conclude that the flare is a "bald patch flare," which is produced by a fast reconnection in a vertical current sheet forming near the bald patch as a result of the deforming of a large shear, while a loss of global equilibrium triggered by this reconnection leads the field to open up for a CME. In their picture, the flare is interpreted as energy release near the bald patch via the current sheet reconnection. In our case, the observations suggest that most flare energy is released via the standard reconnection model, as evidenced by several typical features such as the postflare potential-like loops in EUV and two flare ribbons at the footpoints, while the bald patch plays a role in preflare energy release via a slow reconnection. A key observation is the position of two X-ray jets in coincidence with the bald patch. This suggests that the jets are produced by the reconnection at the bald patch. However, as the jets appear only several minutes before the HXR onset, the separatrix fields may have started to undergo rapid reconnection at this time. After the eruption, a vertical current sheet may develop in the separatrix fields around the bald patch, so the fast reconnection releases a portion of energy producing flamelike brightenings seen in Hα and EUV. However, these brightenings decayed very fast before the flare maximum and were much weaker compared to the strong ribbons developing on the sides of the neutral line near the main spot, suggesting that the energy released around the bald patch appears to be only a small fraction of the total flare energy. This is consistent with the magnetic feature that the field around the bald patch is much weaker and less sheared than that around the neutral line in the EFR N3S3.

In addition, the postflare weak dimmings in EIT near AR 8210 and AR 8214 suggest that the TIL system may be opened only partially for the CME. On the other hand, the opened large-scale fields in the CME may also close back after a time according to the standard model, thus nearly reforming the original configuration, under which further new emerging sheared flux can reproduce flares and CMEs in the same behavior. This can interpret homologous disappearances of transequatorial X-ray loops in the flare CME events on 1998 May 6–9 (Khan & Hudson 2000). Sterling & Moore (2001) also suggested a similar cycle for reconnection between coronal hole fields and EFRs, accounting for the homologous nature of the eruptions.

6. CONCLUSION

Super active regions are often characterized by features such as a large flux-imbalance magnetic structure and a series of surrounding small sheared EFRs (Zhang & Wang 1994; Ishii et al. 1998). The net flux of the super active regions readily forms the large-scale interconnecting field systems with widespread magnetic regions. Our study of a typical case of flare CMEs occurring in such a complicated configuration indicates that slow reconnection at the bald patch between the transequatorial magnetic arch and the local active region arch systems can lead to eruptions of the confined emerging twisted flux system triggering impulsive flares and a subsequent global restructuring of multipolar magnetic systems responsible for explosive CMEs. The opening of the involved large-scale field lines causes surface signatures such as widely extending dimmings in EIT and the X-ray transequatorial loop disappearances. Our study shows that the global restructuring can also cause the dimmings that are not magnetically connected to the flaring active region. The dimming features can be used to estimate mass, magnetic energy, and flux of the ejected material for halo CMEs. Such flare CMEs are supposed to be reproduced in the same manner when a sequence of new emerging twisted flux systems forms around the main magnetic polarity. Finally, we expect to study more cases with similar activity features in the future, using data such as vector magnetic fields and EUV and SXR observations with high spatial and temporal resolutions, to examine the scenario we proposed in this study.

T. W. would like to thank J. X. Wang, H. Hudson, and J. Khan for their valuable suggestions and discussions. T. W. also thanks E. W. Cliver for his kind help. Many thanks to the referee for his many valuable suggestions and comments on this paper. T. W. received support from NSFC under grants 49990450 and 19791090 and also from the Japanese Ministry of Science and Education. T. W. is grateful to all members of the Kwasan and Hida Observatories of Kyoto University for their kind help when he worked there under a postdoctoral fellowship. Y. Y. acknowledges support from CAS, NSFC (49990452, 19973008), and the Ministry of Science and Technology of China (G2000078403). We also thank Kanzelhöhe Solar Observatory for their data contributions on the World Wide Web. NSO/Kitt Peak data used are produced cooperatively by NSF/NOAO, NASA/GSFC, and NOAA/SEL. *SOHO* is a project of international cooperation between ESA and NASA, and *Yohkoh* is a mission of ISAS (Japan) with participation from the US and UK.

REFERENCES

Ai, G., & Hu, Y. 1986, Publ. Beijing Astron. Obs., 8, 1
Altschuler, M. D., & Newkirk, G. 1969, Sol. Phys., 9, 131
Amari, T., Luciani, J. F., Mikic, Z., & Linker, J. 2000, ApJ, 529, L49
Antiochos, S. K. 1998, ApJ, 502, L181
Antiochos, S. K., Devore, C. R., & Klimchuk, J. A. 1999, ApJ, 510, 485
Arfken, G. 1966, Mathematical Methods for Physicists (New York: Academic Press)
Arthur, N. C. 2000, in Allen's Astrophysical Quantities (4th ed.; New York: AIP), 359
Aulanier, G., DeLuca, E. E., Antiochos, S. K., McMullen, R. A., & Golub, L. 2000, ApJ, 540, 1126
Aulanier, G., Schmieder, B., Demoulin, P., van Driel–Gesztelyi, L., & DeForest, C. 1998, in ASP Conf. Ser. 155, Second Advances in Solar Physics Euroconference: Three-dimensional Structure of Solar Active Regions, ed. C. E. Alissandrakis & B. Schmieder (San Francisco: ASP), 105
Brebbia, C. A., Telles, J. C. F., & Wrobel, L. C. 1984, Boundary Element Techniques (Berlin: Springer)

Brueckner, G. E., et al. 1995, Sol. Phys., 162, 357
Courant, R., & Hilbert, D. 1962, Methods of Mathematical Physics, Vol. 2 (New York: Wiley)
Delaboudinière, J.-P., et al. 1995, Sol. Phys., 162, 291
Delannée, C., & Aulanier, G. 1999, Sol. Phys., 190, 107
Delannée, C., Delaboudinière, J.-P., & Lamy, P. 2000, A&A, 355, 725
Dere, K. P., Brueckner, G. E., Howard, R. A., Koomen, M. J., & Korendyke, C. M. 1997, Sol. Phys., 175, 601
Fárník, F., Karlický, M., & Švestka, Z. 1999, Sol. Phys., 187, 33
Hakamada, K., & Kojima, M. 1999, Sol. Phys., 187, 115
Howard, R. A., Sheeley, N. R., Koomen, M. J., & Michels, D. J. 1985, J. Geophys. Res., 90, 8173
Hudson, H. S., Acton, L. W., & Freeland, S. L. 1996, ApJ, 470, 629
Hudson, H. S., Lemen, J. R., St. Cyr, O. C., Sterling, A. C., & Webb, D. F. 1998, Geophys. Res. Lett., 25, 2481
Hundhausen, A. J. 1997, in Coronal Mass Ejections: Geophysical Monograph 99, ed. N. Crooker et al. (Washington, DC: AGU), 1
Ishii, T. T., Kurokawa, H., & Takeuchi, T. T. 1998, ApJ, 499, 898
Kahler, S. 1992, ARA&A, 30, 113
Khan, J. I., & Hudson, H. S. 2000, Geophys. Res. Lett., 27, 1083
Kellogg, O. D. 1953, in Foundation of Potential Theory (Dover: New York), 247
Klimchuk, J. A., & Sturrock, P. A. 1992, ApJ, 385, 344
Kosovichev, A. G., & Zharkova, V. V. 1999, Sol. Phys., 190, 459
Kosugi, T., et al. 1991, Sol. Phys., 136, 17
Leka, K. D., Canfield, R. C., McClymont, A. N., & van Driel–Gesztelyi, L. 1996, ApJ, 462, 547
Lin, J., & Forbes, T. G. 2000, J. Geophys. Res., 105, 2375
Lyons, M. A., & Simnett, G. M. 1999, Sol. Phys., 186, 363
Maia, D., Vourlidas, A., Pick, M., Howard, R., Schwenn, R., & Magalhães, A. 1999, J. Geophys. Res., 104, 12507
Moreton, G. E. 1960, AJ, 65, 494
Newkirk, G., Altschuler, M. D., & Harvey, J. W. 1968, in IAU Symp. 35, Structure and Development of Solar Active Regions, ed. K. O. Kiepenheuer (Dordrecht: Kluwer), 379
Nitta, N., & Akiyama, S. 1999, ApJ, 525, L57
Ohyama, M., & Shibata, K. 1998, ApJ, 499, 934
Pevtsov, A. A. 2000, ApJ, 531, 553
Pick, M., Demoulin, P., Maia, D., & Plunkett, S. 1999a, in The 9th European Meeting on Solar Physics, Magnetic Fields and Solar Processes, ed. A. Wilson (ESA SP-448; Noordwijk: ESA), 915
Pick, M., Maia, D., Vourlidas, A., Benz, A. O., Howard, R., & Thompson, B. J. 1999b, in Solar Wind Nine, Proceedings of the Ninth International Solar Wind Conference, ed. S. R. Habbal et al. (AIP-471; New York: AIP), 649
Pohjolainen, S., et al. 2001, ApJ, 556, 421
Pohjolainen, S., Khan, J. I., & Vilmer, N. 1999, in The 9th European Meeting on Solar Physics, Magnetic Fields and Solar Processes (ESA SP-448; Noordwijk: ESA), 991
Poletto, G., & Kopp, R. A. 1988, Sol. Phys., 116, 163
Press, W. H., Teukolsky, S. A., Vetterling, W. T., & Flannery, B. P. 1994, Numerical Recipes in Fortran (2d ed.; Cambridge: Cambridge Univ. Press), 634
Sakurai, T. 1982, Sol. Phys., 76, 301
Schatten, K. H., Wilcox, J. M., & Ness, N. F. 1969, Sol. Phys., 6, 442
Scherrer, P. H., et al. 1995, Sol. Phys., 162, 129
Shibata, K., et al. 1995, ApJ, 451, L83
Shibata, K., Yokoyama, T., & Shimojo, M. 1996, Adv. Space Res., 17, 197
Sterling, A. C., & Hudson, H. S. 1997, ApJ, 491, L55
Sterling, A. C., Hudson, H. S., Thompson, B. J., & Zarro, D. M. 2000, ApJ, 532, 628
Sterling, A. C., & Moore, R. L. 2001, ApJ, 560, 1045
Švestka, Z. 1981, in Solar Flare Magnetohydrodynamics, ed. E. R. Priest (New York: Gordon and Breach), 47
Thompson, B. J., Cliver, E. W., Nitta, N., Delannée, C., & Delaboudinière, J.-P. 2000, Geophys. Res. Lett., 27, 1431
Titov, V. S., & Démoulin, P. 1999, A&A, 351, 707
Tsuneta, S., et al. 1991, Sol. Phys., 136, 37
Uchida, Y., Altschuler, D., & Newkirk, G., Jr. 1973, Sol. Phys., 28, 495
Vourlidas, A., Subramanian, P., Dere, K. P., & Howard, R. A. 2000, ApJ, 534, 456
Wang, J., Shi, Z., Wang, H., & Lü, Y. 1996, ApJ, 456, 861
Wang, T. J., & Abramenko, V. I. 2000, A&A, 357, 1056
Wang, T. J., Wang, H. N., & Qiu, J. 1999, A&A, 342, 854
Wang, T. J., Xu, A. A., & Zhang, H. Q. 1994, Sol. Phys., 155, 99
Wang, Y.-M., & Sheeley, N. R., Jr. 1992, ApJ, 392, 310
Warmuth, A., Hanslmeier, A., Messerotti, M., Cacciani, A., Moretti, P. F., & Otruba, W. 2000, Sol. Phys., 194, 103
Webb, D. F., & Hundhausen, A. J. 1987, Sol. Phys., 108, 383
Yan, Y., & Sakurai, T. 2000, Sol. Phys., 195, 89
Yan, Y., Yu, Q., & Kang, F. 1991, Sol. Phys., 136, 195
Yan, Y., Yu, Q., & Shi, H. 1993, in Advances in Boundary Element Techniques, ed. J. H. Kane, G. Maier, N. Tosaka, & S. N. Atluri (New York: Springer), 447
Yokoyama, T., & Shibata, K. 1995, Nature, 375, 42
Zarro, D. M., Sterling, A. C., Thompson, B. J., Hudson, H. S., & Nitta, N. 1999, ApJ, 520, L139
Zhang, H. Q., & Wang, T. J. 1994, Sol. Phys., 151, 129
Zhang, J., Wang, J. X., & Nitta, N. 2001, Chinese J. Astron. Astrophys., 1, 85
Zhao, X., Hoeksema, J. T., & Scherrer, P. H. 1997, in Proceedings of the Fifth *SOHO* Workshop, The Corona and Solar Wind near Maximum Activity, ed. A. Wilson (ESA SP-404; Noordwijk: ESA), 751
Zheleznyakov, V. V. 1970, Radio Emission of the Sun and Planets (Oxford: Pergamon Press)